

1      **High-level cognition during story listening is reflected in  
2      high-order dynamic correlations in neural activity patterns**

3      Lucy L. W. Owen<sup>1</sup>, Thomas H. Chang<sup>1,2</sup>, and Jeremy R. Manning<sup>1,†</sup>

<sup>1</sup>Department of Psychological and Brain Sciences,  
Dartmouth College, Hanover, NH

<sup>2</sup>Amazon.com, Seattle, WA

†Address correspondence to jeremy.r.manning@dartmouth.edu

4      August 11, 2021

5      **Abstract**

6      Our thoughts arise from coordinated patterns of interactions between brain structures that change  
7      with our ongoing experiences. High-order dynamic correlations in neural activity patterns reflect different  
8      subgraphs of the brain’s functional connectome that display homologous lower-level dynamic correlations.  
9      Here we test the hypothesis that high-level cognition is reflected in high-order dynamic correlations in brain  
10     activity patterns. We develop an approach to estimating high-order dynamic correlations in timeseries data,  
11     and we apply the approach to neuroimaging data collected as human participants either listen to a ten-  
12     minute story or listen to a temporally scrambled version of the story. We train across-participant pattern  
13     classifiers to decode (in held-out data) when in the session each neural activity snapshot was collected. We  
14     find that classifiers trained to decode from high-order dynamic correlations yield the best performance on  
15     data collected as participants listened to the (unscrambled) story. By contrast, classifiers trained to decode  
16     data from scrambled versions of the story yielded the best performance when they were trained using first-  
17     order dynamic correlations or non-correlational activity patterns. We suggest that as our thoughts become  
18     more complex, they are reflected in higher-order patterns of dynamic network interactions throughout the  
19     brain.

20     **Introduction**

21     A central goal in cognitive neuroscience is to elucidate the neural code: i.e., the mapping between (a) mental  
22     states or cognitive representations and (b) neural activity patterns. One means of testing models of the  
23     neural code is to ask how accurately that model is able to “translate” neural activity patterns into known  
24     (or hypothesized) mental states or cognitive representations<sup>1–9</sup>. Training decoding models on different  
25     types of neural features (Fig. 1a) can also help to elucidate which specific aspects of neural activity patterns  
26     are informative about cognition and, by extension, which types of neural activity patterns might compose  
27     the neural code. For example, prior work has used region of interest analyses to estimate the anatomical  
28     locations of specific neural representations<sup>10</sup>, or to compare the relative contributions to the neural code  
29     of multivariate activity patterns versus dynamic correlations between neural activity patterns<sup>11,12</sup>. An

30 emerging theme in this literature is that cognition is mediated by dynamic interactions between brain  
31 structures<sup>13–25</sup>.

32 [Figure 1 about here.]

33 Studies of the neural code to date have primarily focused on univariate or multivariate neural patterns<sup>2</sup>,  
34 or (more recently) on patterns of dynamic first-order correlations (i.e., interactions between pairs of brain  
35 structures<sup>11,12,18,20–22</sup>). What might the future of this line of work hold? For example, is the neural code  
36 implemented through higher-order interactions between brain structures<sup>26</sup>? Second-order correlations re-  
37 flect homologous patterns of correlation. In other words, if the dynamic patterns of correlations between  
38 two regions, *A* and *B*, are similar to those between two other regions, *C* and *D*, this would be reflected  
39 in the second-order correlations between (*A*–*B*) and (*C*–*D*). In this way, second-order correlations identify  
40 similarities and differences between subgraphs of the brain’s connectome. Analogously, third-order cor-  
41 relations reflect homologies between second-order correlations—i.e., homologous patterns of homologous  
42 interactions between brain regions. More generally, higher-order correlations reflect homologies between  
43 patterns of lower-order correlations. We can then ask: which “orders” of interaction are most reflective of  
44 high-level cognitive processes?

45 One reason one might expect to see homologous networks in a dataset is related to the notion that  
46 network dynamics reflect ongoing neural computations or cognitive processing<sup>27</sup>. If the nodes in two brain  
47 networks are interacting (within each network) in similar ways then, according to our characterization  
48 of network dynamics, we refer to the similarities between those patterns of interaction as higher-order  
49 correlations. When higher-order correlations are themselves changing over time, we can also attempt to  
50 capture and characterize those high-order dynamics.

51 Another central question pertains to the extent to which the neural code is carried by activity patterns  
52 that directly reflect ongoing cognition<sup>1,2</sup>, versus the dynamic properties of the network structure itself,  
53 independent of specific activity patterns in any given set of regions<sup>16</sup>. For example, graph measures  
54 such as centrality and degree<sup>28</sup> may be used to estimate how a given brain structure is “communicating”  
55 with other structures, independently of the specific neural representations carried by those structures.  
56 If one considers a brain region’s position in the network (e.g., its eigenvector centrality) as a dynamic  
57 property, one can compare how the positions of different regions are correlated, and/or how those patterns  
58 of correlations change over time. We can also compute higher-order patterns in these correlations to  
59 characterize homologous subgraphs in the connectome that display similar changes in their constituent  
60 brain structures’ interactions with the rest of the brain.

61 To gain insights into the above aspects of the neural code, we developed a computational framework

for estimating dynamic high-order correlations in timeseries data. This framework provides an important advance, in that it enables us to examine patterns of higher-order correlations that are computationally intractable to estimate via conventional methods. Given a multivariate timeseries, our framework provides timepoint-by-timepoint estimates of the first-order correlations, second-order correlations, and so on. Our approach combines a kernel-based method for computing dynamic correlations in timeseries data with a dimensionality reduction step (Fig. 1b) that projects the resulting dynamic correlations into a low-dimensional space. We explored two dimensionality reduction approaches: principle components analysis<sup>29</sup> (PCA), which preserves an approximately invertible transformation back to the original data<sup>30-32</sup>, and a second non-invertible algorithm for computing dynamic patterns in eigenvector centrality<sup>33</sup>. This latter approach characterizes correlations between each feature dimension's relative position in the network (at each moment in time) in favor of the specific activity histories of different features<sup>26,34,35</sup>.

We validated our approach using synthetic data where the underlying correlations were known. We then applied our framework to a neuroimaging dataset collected as participants listened to either an audio recording of a ten-minute story, listened to a temporally scrambled version of the story, or underwent a resting state scan<sup>36</sup>. Temporal scrambling has been used in a growing number of studies, largely by Uri Hasson's group, to identify brain regions that are sensitive to higher-order and longer-timescale information (e.g., cross-sensory integration, rich narrative meaning, complex situations, etc.) versus regions that are primarily sensitive to low-order (e.g., sensory) information. For example,<sup>37</sup> argues that when brain areas are sensitive to fine versus coarse temporal scrambling, this indicates that they are "higher order" in the sense that they process contextual information pertaining to further-away timepoints. By contrast, low-level regions, such as primary sensory cortices, do not meaningfully change their responses (after correcting for presentation order) even when the stimulus is scrambled at fine timescales.

We used a subset of the story listening and rest data to train across-participant classifiers to decode listening times (of groups of participants) using a blend of neural features (comprising neural activity patterns, as well as different orders of dynamic correlations between those patterns that were inferred using our computational framework). We found that both the PCA-based and eigenvector centrality-based approaches yielded neural patterns that could be used to decode accurately (i.e., well above chance). Both approaches also yielded the best decoding accuracy for data collected during (intact) story listening when high-order (PCA: second-order; eigenvector centrality: fourth-order) dynamic correlation patterns were included as features. When we trained classifiers on the scrambled stories or resting state data, only (relatively) lower-order dynamic patterns were informative to the decoders. Taken together, our results indicate that high-level cognition is supported by high-order dynamic patterns of communication between brain structures.

95 **Results**

96 We sought to understand whether high-level cognition is reflected in dynamic patterns of high-order correla-  
97 tions. To that end, we developed a computational framework for estimating the dynamics of stimulus-driven  
98 high-order correlations in multivariate timeseries data (see Dynamic inter-subject functional connectivity  
99 (DISFC) and Dynamic higher-order correlations). We evaluated the efficacy of this framework at recovering  
100 known patterns in several synthetic datasets (see Synthetic data: simulating dynamic first-order corre-  
101 lations and Synthetic data: simulating dynamic higher-order correlations). We then applied the framework  
102 to a public fMRI dataset collected as participants listened to an auditorily presented story, listened to a  
103 temporally scrambled version of the story, or underwent a resting state scan (see Functional neuroimaging  
104 data collected during story listening). We used the relative decoding accuracies of classifiers trained on  
105 different sets of neural features to estimate which types of features reflected ongoing cognitive processing.

106 **Recovering known dynamic first-order correlations**

107 We generated synthetic datasets that differed in how the underlying first-order correlations changed over  
108 time. For each dataset, we applied Equation 4 with a variety of kernel shapes and widths. We assessed how  
109 well the true underlying correlations at each timepoint matched the recovered correlations (Fig. 2). For every  
110 kernel and dataset we tested, our approach recovered the correlation dynamics we embedded into the data.  
111 However, the quality of these recoveries varied across different synthetic datasets in a kernel-dependent  
112 way.

113 [Figure 2 about here.]

114 In general, wide monotonic kernel shapes (Laplace, Gaussian), and wider kernels (within a shape),  
115 performed best when the correlations varied gradually from moment-to-moment (Figs. 2a, c, and d). In the  
116 extreme, as the rate of change in correlations approaches 0 (Fig. 2a), an infinitely wide kernel would exactly  
117 recover the Pearson's correlation (e.g., compare Eqns. 1 and 4).

118 When the correlation dynamics were unstructured in time (Fig. 2b), a Dirac  $\delta$  kernel (infinitely narrow)  
119 performed best. This is because, when every timepoint's correlations are independent of the correlations at  
120 every other timepoint, averaging data over time dilutes the available signal. Following a similar pattern,  
121 holding kernel shape fixed, narrower kernel parameters better recovered randomly varying correlations.

122 **Recovering known dynamic higher-order correlations**

123 Following our approach to evaluating our ability to recover known dynamic first-order correlations from  
124 synthetic data, we generated an analogous second set of synthetic datasets that we designed to exhibit  
125 known dynamic first-order and second-order correlations (see Synthetic data: simulating dynamic higher-  
126 order correlations). We generated a total of 400 datasets (100 datasets for each category) that varied in how  
127 the first-order and second-order correlations changed over time. We then repeatedly applied Equation 4  
128 using the overall best-performing kernel from our first-order tests (a Laplace kernel with a width of 20;  
129 Fig. 2) to assess how closely the recovered dynamic correlations matched the dynamic correlations we had  
130 embedded into the datasets.

131 Overall, we found that we could reliably recover both first-order and second-order correlations from the  
132 synthetic data (Fig. 3). When the correlations were stable for longer intervals, or changed gradually (constant,  
133 ramping, and event datasets), recovery performance was relatively high, and we were better able to recover  
134 dynamic first-order correlations than second-order correlations. This is because errors in our estimation  
135 procedure at lower orders necessarily propagate to higher orders (since lower-order correlations are used to  
136 estimate higher-order correlations). Conversely, when the correlations were particularly unstable (random  
137 datasets), we better recovered second-order correlations. This is because noise in our data generation  
138 procedure propagates from higher orders to lower orders (see Synthetic data: simulating dynamic high-  
139 order correlations).

140 [Figure 3 about here.]

141 We also examined the impact of the data duration (Fig. S3) and complexity (number of zero-order features;  
142 Fig. S4) on our ability to accurately recover ground truth first-order and second-order dynamic correlations.  
143 In general, we found that our approach better recovers ground truth dynamic correlations from longer  
144 duration timeseries data. We also found that our approach tends to best recover data generated using fewer  
145 zero-order features (i.e., lower complexity), although this tendency was not strictly monotonic. Further,  
146 because our data generation procedure requires  $O(K^4)$  memory to generate a second-order timeseries with  $K$   
147 zero-order features, we were not able to fully explore how the number of zero-order features affects recovery  
148 accuracy as the number of features gets larger (e.g., as it approaches the number of features present in the  
149 fMRI data we examine below). Although we were not able to formally test this to our satisfaction, we expect  
150 that accurately estimating dynamic high-order correlations would require data with many more zero-order  
151 features than we were able to simulate. Our reasoning is that high-order correlations necessarily involve  
152 larger numbers of lower-order features, so achieving adequate “resolution” high-order timeseries might  
153 require many low-order features.

154 Taken together, our explorations using synthetic data indicated that we are able to partially, but not  
155 perfectly, recover ground truth dynamic first-order and second-order correlations. This suggests that our  
156 modeling approach provides a meaningful (if noisy) estimate of high-order correlations. We next turned  
157 to analyses of human fMRI data to examine whether the recovered dynamics might reflect the dynamics of  
158 human cognition during a naturalistic story-listening task.

159 **Cognitively relevant dynamic high-order correlations in fMRI data**

160 We used across-participant temporal decoders to identify cognitively relevant neural patterns in fMRI data  
161 (see Forward inference and decoding accuracy). The dataset we examined<sup>36</sup> comprised four experimental  
162 conditions that exposed participants to stimuli that varied systematically in how cognitively engaging they  
163 were. The intact experimental condition (intact) had participants listen to an audio recording of a 10-minute  
164 story. The paragraph-scrambled experimental condition (paragraph) had participants listen to a temporally  
165 scrambled version of the story, where the paragraphs occurred out of order (but where the same total set of  
166 paragraphs were presented over the full listening interval). All participants in this condition experienced  
167 the scrambled paragraphs in the same order. The word-scrambled experimental condition (word) had  
168 participants listen to a temporally scrambled version of the story where the words in the story occurred  
169 in a random order. All participants in the word condition experienced the scrambled words in the same  
170 order. Finally, in a rest experimental condition (rest), participants lay in the scanner with no overt stimulus,  
171 with their eyes open (blinking as needed). This public dataset provided a convenient means of testing our  
172 hypothesis that different levels of cognitive processing and engagement are reflected in different orders of  
173 brain activity dynamics.

174 [Figure 4 about here.]

175 In brief, we computed timeseries of dynamic high-order correlations that were similar across participants  
176 in each of two randomly assigned groups: a training group and a test group. We then trained classifiers  
177 on the training group's data to match each sample from the test group with a stimulus timepoint. Each  
178 classifier comprised a weighted blend of neural patterns that reflected up to  $n^{\text{th}}$ -order dynamic correlations  
179 (see Feature weighting and testing). We repeated this process for  $n \in \{0, 1, 2, \dots, 10\}$ . Our examinations of  
180 synthetic data suggested that none of the kernels we examined were “universal” in the sense of optimally  
181 recovering underlying correlations regardless of the temporal structure of those correlations. We found a  
182 similar pattern in the (real) fMRI data, whereby different kernels yielded different decoding accuracies, but  
183 no single kernel emerged as the clear “best.” In our analyses of neural data, we therefore averaged our

184 decoding results over a variety of kernel shapes and widths in order to identify results that were robust to  
185 specific kernel parameters (see Identifying robust decoding results).

186 Our approach to estimating dynamic high-order correlations entails mapping the high-dimensional  
187 feature space of correlations (represented by a  $T$  by  $O(K^2)$  matrix) onto a lower-dimensional feature space  
188 (represented by a  $T$  by  $K$  matrix). We carried out two sets of analyses that differed in how this mapping was  
189 computed. The first set of analyses used PCA to find a low-dimensional embedding of the original dynamic  
190 correlation matrices (Fig. 4a,b). The second set of analyses characterized correlations in dynamics of each  
191 feature's eigenvector centrality, but did not preserve the underlying activity dynamics (Fig. 4c,d).

192 [Figure 5 about here.]

193 Both sets of temporal decoding analyses yielded qualitatively similar results for the auditory (non-rest)  
194 conditions of the experiment (Fig. 4: pink, green, and teal lines; Fig. 5: three leftmost columns). The highest  
195 decoding accuracy for participants who listened to the intact (unscrambled) story was achieved using high-  
196 order dynamic correlations (PCA: second-order; eigenvector-centrality: fourth-order). Scrambled versions  
197 of the story were best decoded by lower-order correlations (PCA/paragraph: first-order; PCA/word: order  
198 zero; eigenvector centrality/paragraph: order zero; eigenvector centrality/word: order zero). The two sets  
199 of analyses yielded different decoding results on resting state data (Fig. 4: purple lines; Fig. 5: rightmost  
200 column). We note that, while the resting state times could be decoded reliably, the accuracies were only very  
201 slightly above chance. We speculate that the decoders might have picked up on attentional drift, boredom,  
202 or tiredness; we hypothesize that these all increased throughout the resting state scan. The decoders might  
203 be picking up on aspects of these loosely defined cognitive states that are common across individuals. The  
204 PCA-based approach achieved the highest resting state decoding accuracy using order zero features (non-  
205 correlational, activation-based), whereas the eigenvector centrality-based approach achieved the highest  
206 resting state decoding accuracy using second-order correlations. Taken together, these analyses indicate  
207 that high-level cognitive processing (while listening to the intact story) is reflected in the dynamics of high-  
208 order correlations in brain activity, whereas lower-level cognitive processing (while listening to scrambled  
209 versions of the story that lack rich meaning) is reflected in the dynamics of lower-order correlations and  
210 non-correlational activity dynamics. Further, these patterns are associated both with the underlying activity  
211 patterns (characterized using PCA) and also with the changing relative positions that different brain areas  
212 occupy in their associated networks (characterized using eigenvector centrality).

213 [Figure 6 about here.]

214 Having established that patterns of high-order correlations are informative to decoders, we next won-  
215 dered which specific networks of brain regions contributed most to these patterns. As a representative

example, we selected the kernel parameters that yielded decoding accuracies that were the most strongly correlated (across conditions and orders) with the average accuracies across all of the kernel parameters we examined. Using Figure 4c as a template, the best-matching kernel was a Laplace kernel with a width of 50 (Fig. 9d; also see Fig. S9). We used this kernel to compute a single  $K$  by  $K$   $n^{\text{th}}$ -order DISFC matrix for each experimental condition. We then used Neurosynth<sup>38</sup> to compute the terms most highly associated with the most strongly correlated pairs of regions in each of these matrices (Fig. 6; see Reverse inference).

For all of the story listening conditions (intact, paragraph, and word; top three rows of Fig. 6), we found that first- and second-order correlations were most strongly associated with auditory and speech processing areas. During intact story listening, third-order correlations reflected integration with visual areas, and fourth-order correlations reflected integration with areas associated with high-level cognition and cognitive control, such as the ventrolateral prefrontal cortex. However, when participants listened to temporally scrambled stories, these higher-order correlations instead involved interactions with additional regions associated with speech and semantic processing (second and third rows of Fig. 6). By contrast, we found a much different set of patterns in the resting state data (Fig. 6, bottom row). First-order resting state correlations were most strongly associated with regions involved in counting and numerical understanding. Second-order resting state correlations were strongest in visual areas; third-order correlations were strongest in task-positive areas; and fourth-order correlations were strongest in regions associated with autobiographical and episodic memory. We carried out analogous analyses to create maps (and decode the top associated Neurosynth terms) for up to fifteenth-order correlations (Figs. S5, S6, S7, and S8). Of note, examining fifteenth-order correlations between 700 nodes using conventional methods would have required storing roughly  $\frac{700^{2 \times 15}}{2} \approx 1.13 \times 10^{85}$  floating point numbers—assuming single-precision (32 bits each), this would require roughly 32 times as many bits as there are molecules in the known universe! Although these fifteenth-order correlations do appear (visually) to have some well-formed structure, we provide this latter example primarily as a demonstration of the efficiency and scalability of our approach.

## Discussion

We tested the hypothesis that high-level cognition is reflected in high-order brain network dynamics<sup>19,26</sup>. We examined high-order network dynamics in functional neuroimaging data collected during a story listening experiment. When participants listened to an auditory recording of the story, participants exhibited similar high-order brain network dynamics. By contrast, when participants instead listened to temporally scrambled recordings of the story, only lower-order brain network dynamics were similar across participants. Our results indicate that higher orders of network interactions support higher-level aspects of cognitive

247 processing (Fig. 7).

248 [Figure 7 about here.]

249 The notion that cognition is reflected in (and possibly mediated by) patterns of first-order network dy-  
250 namics has been suggested by or proposed in myriad empirical studies and reviews<sup>11,12,17,18,20–22,24,25,32,39–42</sup>.  
251 Our study extends this line of work by finding cognitively relevant higher-order network dynamics that  
252 reflect ongoing cognition. Our findings also complement other work that uses graph theory and topology  
253 to characterize how brain networks reconfigure during cognition<sup>16,26,30,31,34,35,43</sup>.

254 An open question not addressed by our study pertains to how different structures integrate incoming  
255 information with different time constants. For example, one line of work suggests that the cortical surface  
256 comprises a structured map such that nearby brain structures process incoming information at similar  
257 timescales. Low-level sensory areas integrate information relatively quickly, whereas higher-level regions  
258 integrate information relatively slowly<sup>37,44–49</sup>. A similar hierarchy appears to play a role in predicting future  
259 events<sup>50</sup>. Other related work in human and mouse brains indicates that the temporal response profile of a  
260 given brain structure may relate to how strongly connected that structure is with other brain areas<sup>51</sup>. Further  
261 study is needed to understand the role of temporal integration at different scales of network interaction,  
262 and across different anatomical structures. Importantly, our analyses do not speak to the physiological  
263 basis of higher-order dynamics, and could reflect nonlinearities, chaotic patterns, non-stationarities, and/or  
264 multistability, etc. However, our decoding analyses do indicate that higher-order dynamics are consistent  
265 across individuals, and therefore unlikely to reflect non-stimulus-driven dynamics that are unlikely to be  
266 similar across individuals.

267 One limitation of our approach relates to how noise propagates in our estimation procedure. Specifi-  
268 cally, our procedure for estimating high-order dynamic correlations depends on estimates of lower-order  
269 dynamic correlations. This means that our measures of which higher-order patterns are reliable and stable  
270 across experimental conditions are partially confounded with the stability of lower-order patterns. Prior  
271 work suggests that the stability of what we refer to here as first-order dynamics likely varies across the  
272 experimental conditions we examined<sup>36</sup>. Therefore a caveat to our claim that richer stimuli evoke more  
273 stable higher-order dynamics is that our approach assumes that those high-order dynamics reflect relations  
274 or interactions between lower-order features.

275 Another potential limitation of our approach relates to recent work suggesting that the brain undergoes  
276 rapid state changes, for example across event boundaries<sup>44,52</sup> used hidden semi-Markov models to estimate  
277 state-specific network dynamics<sup>53</sup>. Our general approach might be extended by considering putative state  
278 transitions. For example, rather than weighting all timepoints using a similar kernel (Eqn. 4), the kernel

279 function could adapt on a timepoint-by-timepoint basis such that only timepoints determined to be in the  
280 same “state” were given non-zero weight.

281 Identifying high-order network dynamics associated with high-level cognition required several im-  
282 portant methods advances. First, we used kernel-based dynamic correlations to extended the notion of  
283 (static) inter-subject functional connectivity<sup>36</sup> to a dynamic measure of inter-subject functional connectivity  
284 (DISFC) that does not rely on sliding windows<sup>11</sup>, and that may be computed at individual timepoints. This  
285 allowed us to precisely characterize stimulus-evoked network dynamics that were similar across individ-  
286 uals. Second, we developed a computational framework for efficiently and scalably estimating high-order  
287 dynamic correlations. Our approach uses dimensionality reduction algorithms and graph measures to  
288 obtain low-dimensional embeddings of patterns of network dynamics. Third, we developed an analysis  
289 framework for identifying robust decoding results by carrying out our analyses using a range of parameter  
290 values and identifying which results were robust to specific parameter choices. By showing that high-level  
291 cognition is reflected in high-order network dynamics, we have elucidated the next step on the path towards  
292 understanding the neural basis of cognition.

## 293 Methods

294 Our general approach to efficiently estimating high-order dynamic correlations comprises four general  
295 steps (Fig. 8). First, we derive a kernel-based approach to computing dynamic pairwise correlations in  
296 a  $T$  (timepoints) by  $K$  (features) multivariate timeseries,  $\mathbf{X}_0$ . This yields a  $T$  by  $O(K^2)$  matrix of dynamic  
297 correlations,  $\mathbf{Y}_1$ , where each row comprises the upper triangle and diagonal of the correlation matrix at  
298 a single timepoint, reshaped into a row vector (this reshaped vector is  $(\frac{K^2-K}{2} + K)$ -dimensional). Second,  
299 we apply a dimensionality reduction step to project the matrix of dynamic correlations back onto a  $K$ -  
300 dimensional space. This yields a  $T$  by  $K$  matrix,  $\mathbf{X}_1$ , that reflects an approximation of the dynamic correlations  
301 reflected in the original data. Third, we use repeated applications of the kernel-based dynamic correlation  
302 step to  $\mathbf{X}_n$  and the dimensionality reduction step to the resulting  $\mathbf{Y}_{n+1}$  to estimate high-order dynamic  
303 correlations. Each application of these steps to a  $T$  by  $K$  time series  $\mathbf{X}_n$  yields a  $T$  by  $K$  matrix,  $\mathbf{X}_{n+1}$ , that  
304 reflects the dynamic correlations between the columns of  $\mathbf{X}_n$ . In this way, we refer to  $n$  as the order of the  
305 timeseries, where  $\mathbf{X}_0$  (order 0) denotes the original data and  $\mathbf{X}_n$  denotes (approximated)  $n^{\text{th}}$ -order dynamic  
306 correlations between the columns of  $\mathbf{X}_0$ . Finally, we use a cross-validation-based decoding approach to  
307 evaluate how well information contained in a given order (or weighted mixture of orders) may be used  
308 to decode relevant cognitive states. If including a given  $\mathbf{X}_n$  in the feature set yields higher classification  
309 accuracy on held-out data, we interpret this as evidence that the given cognitive states are reflected in

310 patterns of  $n^{\text{th}}$ -order correlations.

311 All of the code used to produce the figures and results in this manuscript, along with links to the  
 312 corresponding datasets, may be found at [github.com/ContextLab/timecorr-paper](https://github.com/ContextLab/timecorr-paper). In addition, we have  
 313 released a Python toolbox for computing dynamic high-order correlations in timeseries data; our toolbox  
 314 may be found at [timecorr.readthedocs.io](https://timecorr.readthedocs.io).

315 [Figure 8 about here.]

### 316 Kernel-based approach for computing dynamic correlations

Given a  $T$  by  $K$  matrix of observations,  $\mathbf{X}$ , we can compute the (static) Pearson's correlation between any pair of columns,  $\mathbf{X}(\cdot, i)$  and  $\mathbf{X}(\cdot, j)$  using<sup>29</sup>:

$$\text{corr}(\mathbf{X}(\cdot, i), \mathbf{X}(\cdot, j)) = \frac{\sum_{t=1}^T (\mathbf{X}(t, i) - \bar{\mathbf{X}}(\cdot, i))(\mathbf{X}(t, j) - \bar{\mathbf{X}}(\cdot, j))}{\sqrt{\sum_{t=1}^T \sigma_{\mathbf{X}(\cdot, i)}^2 \sigma_{\mathbf{X}(\cdot, j)}^2}}, \text{ where} \quad (1)$$

$$\bar{\mathbf{X}}(\cdot, k) = \frac{1}{T} \sum_{t=1}^T \mathbf{X}(t, k), \text{ and} \quad (2)$$

$$\sigma_{\mathbf{X}(\cdot, k)}^2 = \frac{1}{T} \sum_{t=1}^T (\mathbf{X}(t, k) - \bar{\mathbf{X}}(\cdot, k))^2 \quad (3)$$

317 We can generalize this formula to compute time-varying correlations by incorporating a kernel function that  
 318 takes a time  $t$  as input, and returns how much the observed data at each timepoint  $\tau \in [-\infty, \infty]$  contributes  
 319 to the estimated instantaneous correlation<sup>54</sup> at time  $t$  (Fig. 9).

320 [Figure 9 about here.]

Given a kernel function  $\kappa_t(\cdot)$  for timepoint  $t$ , evaluated at timepoints  $\tau \in [1, \dots, T]$ , we can update the static correlation formula in Equation 1 to estimate the instantaneous correlation at timepoint  $t$ :

$$\text{timecorr}_{\kappa_t}(\mathbf{X}(\cdot, i), \mathbf{X}(\cdot, j)) = \frac{\sum_{\tau=1}^T (\mathbf{X}(\tau, i) - \tilde{\mathbf{X}}_{\kappa_t}(\cdot, i))(\mathbf{X}(\tau, j) - \tilde{\mathbf{X}}_{\kappa_t}(\cdot, j))}{\sqrt{\sum_{\tau=1}^T \tilde{\sigma}_{\kappa_t}^2(\mathbf{X}(\cdot, i)) \tilde{\sigma}_{\kappa_t}^2(\mathbf{X}(\cdot, j))}}, \text{ where} \quad (4)$$

$$\tilde{\mathbf{X}}_{\kappa_t}(\cdot, k) = \sum_{\tau=1}^T \kappa_t(\tau) \mathbf{X}(\tau, k), \quad (5)$$

$$\tilde{\sigma}_{\kappa_t}^2(\mathbf{X}(\cdot, k)) = \sum_{\tau=1}^T (\mathbf{X}(\tau, k) - \tilde{\mathbf{X}}_{\kappa_t}(\cdot, k))^2. \quad (6)$$

321 Here  $\text{timecorr}_{\kappa_t}(\mathbf{X}(\cdot, i), \mathbf{X}(\cdot, j))$  reflects the correlation at time  $t$  between columns  $i$  and  $j$  of  $\mathbf{X}$ , estimated using  
 322 the kernel  $\kappa_t$ . We evaluate Equation 4 in turn for each pair of columns in  $\mathbf{X}$  and for kernels centered on each

323 timepoint in the timeseries, respectively, to obtain a  $T$  by  $K$  by  $K$  timeseries of dynamic correlations,  $\mathbf{Y}$ . For  
 324 convenience, we then reshape the upper triangles and diagonals of each timepoint's symmetric correlation  
 325 matrix into a row vector to obtain an equivalent  $T$  by  $(\frac{K^2-K}{2} + K)$  matrix.

326 **Dynamic inter-subject functional connectivity (DISFC)**

Equation 4 provides a means of taking a single observation matrix,  $\mathbf{X}_n$  and estimating the dynamic correlations from moment to moment,  $\mathbf{Y}_{n+1}$ . Suppose that one has access to a set of multiple observation matrices that reflect the same phenomenon. For example, one might collect neuroimaging data from several experimental participants, as each participant performs the same task (or sequence of tasks). Let  $\mathbf{X}_n^1, \mathbf{X}_n^2, \dots, \mathbf{X}_n^P$  reflect the  $T$  by  $K$  observation matrices ( $n = 0$ ) or reduced correlation matrices ( $n > 0$ ) for each of  $P$  participants in an experiment. We can use inter-subject functional connectivity<sup>36,55</sup> (ISFC) to compute the stimulus-driven correlations reflected in the multi-participant dataset at a given timepoint  $t$  using:

$$\bar{\mathbf{C}}(t) = M \left( R \left( \frac{1}{2P} \sum_{p=1}^P Z(\mathbf{Y}_{n+1}^p(t))^\top + Z(\mathbf{Y}_{n+1}^p(t)) \right) \right), \quad (7)$$

where  $M$  extracts and vectorizes the upper triangle and diagonal of a symmetric matrix,  $Z$  is the Fisher  $z$ -transformation<sup>56</sup>:

$$Z(r) = \frac{\log(1+r) - \log(1-r)}{2}, \quad (8)$$

$R$  is the inverse of  $Z$ :

$$R(z) = \frac{\exp(2z-1)}{\exp(2z+1)}, \quad (9)$$

and  $\mathbf{Y}_{n+1}^p(t)$  denotes the correlation matrix at timepoint  $t$  (Eqn. 4) between each column of  $\mathbf{X}_n^p$  and each column of the average  $\mathbf{X}_n$  from all other participants,  $\bar{\mathbf{X}}_n^{\setminus p}$ :

$$\bar{\mathbf{X}}_n^{\setminus p} = \frac{1}{P-1} \sum_{q \in \setminus p} \mathbf{X}_n^q, \quad (10)$$

327 where  $\setminus p$  denotes the set of all participants other than participant  $p$ . In this way, the  $T$  by  $(\frac{K^2-K}{2} + K)$  DISFC  
 328 matrix  $\bar{\mathbf{C}}$  provides a time-varying extension of the ISFC approach developed by<sup>36</sup>.

329 **Low-dimensional representations of dynamic correlations**

330 Given a  $T$  by  $\left(\frac{K^2-K}{2} + K\right)$  matrix of  $n^{\text{th}}$ -order dynamic correlations,  $\mathbf{Y}_n$ , we propose two general approaches  
331 to computing a  $T$  by  $K$  low-dimensional representation of those correlations,  $\mathbf{X}_n$ . The first approach uses  
332 dimensionality reduction algorithms to project  $\mathbf{Y}_n$  onto a  $K$ -dimensional space. The second approach uses  
333 graph measures to characterize the relative positions of each feature ( $k \in [1, \dots, K]$ ) in the network defined  
334 by the correlation matrix at each timepoint.

335 **Dimensionality reduction-based approaches to computing  $\mathbf{X}_n$**

336 The modern toolkit of dimensionality reduction algorithms include Principal Components Analysis<sup>29</sup> (PCA),  
337 Probabilistic PCA<sup>57</sup> (PPCA), Exploratory Factor Analysis<sup>58</sup> (EFA), Independent Components Analysis<sup>59,60</sup>  
338 (ICA),  $t$ -Stochastic Neighbor Embedding<sup>61</sup> ( $t$ -SNE), Uniform Manifold Approximation and Projection<sup>62</sup>  
339 (UMAP), non-negative matrix factorization<sup>63</sup> (NMF), Topographic Factor Analysis<sup>64</sup> (TFA), Hierarchical To-  
340 pographic Factor analysis<sup>11</sup> (HTFA), Topographic Latent Source Analysis<sup>65</sup> (TLSA), dictionary learning<sup>66,67</sup>,  
341 and deep auto-encoders<sup>68</sup>, among others. While complete characterizations of each of these algorithms is  
342 beyond the scope of the present manuscript, the general intuition driving these approaches is to compute  
343 the  $T$  by  $K$  matrix,  $\mathbf{X}$ , that is closest to the original  $T$  by  $J$  matrix,  $\mathbf{Y}$ , where (typically)  $K \ll J$ . The different  
344 approaches place different constraints on what properties  $\mathbf{X}$  must satisfy and which aspects of the data are  
345 compared (and how) in order to optimize how well  $\mathbf{X}$  approximates  $\mathbf{Y}$ .

346 Applying dimensionality reduction algorithms to  $\mathbf{Y}$  yields an  $\mathbf{X}$  whose columns reflect weighted combi-  
347 nations (or nonlinear transformations) of the original columns of  $\mathbf{Y}$ . This has two main consequences. First,  
348 with each repeated dimensionality reduction, the resulting  $\mathbf{X}_n$  has lower and lower fidelity (with respect to  
349 what the “true”  $\mathbf{Y}_n$  might have looked like without using dimensionality reduction to maintain tractability).  
350 In other words, computing  $\mathbf{X}_n$  is a lossy operation. Second, whereas each column of  $\mathbf{Y}_n$  may be mapped  
351 directly onto specific pairs of columns of  $\mathbf{X}_{n-1}$ , the columns of  $\mathbf{X}_n$  reflect weighted combinations and/or  
352 nonlinear transformations of the columns of  $\mathbf{Y}_n$ . Many dimensionality reduction algorithms are invertible  
353 (or approximately invertible). However, attempting to map a given  $\mathbf{X}_n$  back onto the original feature space  
354 of  $\mathbf{X}_0$  will usually require  $O(TK^{2^n})$  space and therefore becomes intractable as  $n$  or  $K$  grow large.

355 **Graph measure approaches to computing  $\mathbf{X}_n$**

356 The above dimensionality reduction approaches to approximating a given  $\mathbf{Y}_n$  with a lower-dimensional  
357  $\mathbf{X}_n$  preserve a (potentially recombined and transformed) mapping back to the original data in  $\mathbf{X}_0$ . We also  
358 explore graph measures that instead characterize each feature’s relative position in the broader network of

359 interactions and connections. To illustrate the distinction between the two general approaches we explore,  
360 suppose a network comprises nodes  $A$  and  $B$ , along with several other nodes. If  $A$  and  $B$  exhibit uncorrelated  
361 activity patterns, then by definition the functional connection (correlation) between them will be close to  
362 0. However, if  $A$  and  $B$  each interact with other nodes in similar ways, we might attempt to capture those  
363 similarities between  $A$ 's and  $B$ 's interactions with those other members of the network.

364 In general, graph measures take as input a matrix of interactions (e.g., using the above notation, a  $K$   
365 by  $K$  correlation matrix or binarized correlation matrix reconstituted from a single timepoint's row of  $\mathbf{Y}$ ),  
366 and return as output a set of  $K$  measures describing how each node (feature) sits within that correlation  
367 matrix with respect to the rest of the population. Widely used measures include betweenness centrality  
368 (the proportion of shortest paths between each pair of nodes in the population that involves the given  
369 node in question<sup>69–73</sup>); diversity and dissimilarity (characterizations of how differently connected a given  
370 node is from others in the population<sup>74–76</sup>); eigenvector centrality and pagerank centrality (measures of  
371 how influential a given node is within the broader network<sup>77–80</sup>); transfer entropy and flow coefficients  
372 (a measure of how much information is flowing from a given node to other nodes in the network<sup>81,82</sup>);  
373  $k$ -coreness centrality (a measure of the connectivity of a node within its local subgraph<sup>83,84</sup>); within-module  
374 degree (a measure of how many connections a node has to its close neighbors in the network<sup>85</sup>); participation  
375 coefficient (a measure of the diversity of a node's connections to different subgraphs in the network<sup>85</sup>); and  
376 subgraph centrality (a measure of a node's participation in all of the network's subgraphs<sup>86</sup>); among others.

377 For a given graph measure,  $\eta : \mathbb{R}^{K \times K} \rightarrow \mathbb{R}^K$ , we can use  $\eta$  to transform each row of  $\mathbf{Y}_n$  in a way that  
378 characterizes the corresponding graph properties of each column. This results in a new  $T$  by  $K$  matrix,  
379  $\mathbf{X}_n$ , that reflects how the features reflected in the columns of  $\mathbf{X}_{n-1}$  participate in the network during each  
380 timepoint (row).

## 381 Dynamic higher-order correlations

382 Because  $\mathbf{X}_n$  has the same shape as the original data  $\mathbf{X}_0$ , approximating  $\mathbf{Y}_n$  with a lower-dimensional  $\mathbf{X}_n$   
383 enables us to estimate high-order dynamic correlations in a scalable way. Given a  $T$  by  $K$  input matrix, the  
384 output of Equation 4 requires  $O(TK^2)$  space to store. Repeated applications of Equation 4 (i.e., computing  
385 dynamic correlations between the columns of the outputted dynamic correlation matrix) each require  
386 exponentially more space; in general the  $n^{\text{th}}$ -order dynamic correlations of a  $T$  by  $K$  timeseries occupies  
387  $O(TK^{2^n})$  space. However, when we approximate or summarize the output of Equation 4 with a  $T$  by  $K$  matrix  
388 (as described above), it becomes feasible to compute even very high-order correlations in high-dimensional  
389 data. Specifically, approximating the  $n^{\text{th}}$ -order dynamic correlations of a  $T$  by  $K$  timeseries requires only

390  $O(TK^2)$  additional space— the same as would be required to compute first-order dynamic correlations. In  
 391 other words, the space required to store  $n + 1$  multivariate timeseries reflecting up to  $n^{\text{th}}$  order correlations  
 392 in the original data scales linearly with  $n$  using our approach (Fig. 8).

393 **Data**

394 We examined two types of data: synthetic data and human functional neuroimaging data. We constructed  
 395 and leveraged the synthetic data to evaluate our general approach<sup>87</sup>. Specifically, we tested how well  
 396 Equation 4 could be used to recover known dynamic correlations using different choices of kernel ( $\kappa$ ; Fig. 9),  
 397 for each of several synthetic datasets that exhibited different temporal properties. We also simulated higher-  
 398 order correlations and tested how well Equation 4 could recover these correlations using the best kernel from  
 399 the previous synthetic data analyses. We then applied our approach to a functional neuroimaging dataset  
 400 to test the hypothesis that ongoing cognitive processing is reflected in high-order dynamic correlations. We  
 401 used an across-participant classification test to estimate whether dynamic correlations of different orders  
 402 contain information about which timepoint in a story participants were listening to.

403 **Synthetic data: simulating dynamic first-order correlations**

404 We constructed a total of 400 different multivariate timeseries, collectively reflecting a total of 4 qualitatively  
 405 different patterns of dynamic first-order correlations (i.e., 100 datasets reflecting each type of dynamic pat-  
 406 tern). Each timeseries comprised 50 features (dimensions) that varied over 300 timepoints. The observations  
 407 at each timepoint were drawn from a zero-mean multivariate Gaussian distribution with a covariance matrix  
 408 defined for each timepoint as described below. We drew the observations at each timepoint independently  
 409 from the draws at all other timepoints; in other words, for each observation  $s_t \sim \mathcal{N}(\mathbf{0}, \Sigma_t)$  at timepoint  $t$ ,  
 410  $p(s_t) = p(s_t | s_{\setminus t})$ .

**Constant.** We generated data with stable underlying correlations to evaluate how Equation 4 characterized correlation “dynamics” when the ground truth correlations were static. We constructed 100 multivariate timeseries whose observations were each drawn from a single (stable) Gaussian distribution. For each dataset (indexed by  $m$ ), we constructed a random covariance matrix,  $\Sigma_m$ :

$$\Sigma_m = \mathbf{C}\mathbf{C}^\top, \text{ where} \quad (11)$$

$$\mathbf{C}(i, j) \sim \mathcal{N}(0, 1), \text{ and where} \quad (12)$$

411  $i, j \in [1, 2, \dots, 50]$ . In other words, all of the observations (for each of the 300 timepoints) within each dataset  
412 were drawn from a multivariate Gaussian distribution with the same covariance matrix, and the 100 datasets  
413 each used a different covariance matrix.

414 **Random.** We generated a second set of 100 synthetic datasets whose observations at each timepoint were  
415 drawn from a Gaussian distribution with a new randomly constructed (using Eqn. 11) covariance matrix.  
416 Because each timepoint’s covariance matrix was drawn independently from the covariance matrices for all  
417 other timepoints, these datasets provided a test of reconstruction accuracy in the absence of any meaningful  
418 underlying temporal structure in the dynamic correlations underlying the data.

**Ramping.** We generated a third set of 100 synthetic datasets whose underlying correlations changed gradually over time. For each dataset, we constructed two “anchor” covariance matrices using Equation 11,  $\Sigma_{\text{start}}$  and  $\Sigma_{\text{end}}$ . For each of the 300 timepoints in each dataset, we drew the observations from a multivariate Gaussian distribution whose covariance matrix at each timepoint  $t \in [0, \dots, 299]$  was given by

$$\Sigma_t = \left(1 - \frac{t}{299}\right)\Sigma_{\text{start}} + \frac{t}{299}\Sigma_{\text{end}}. \quad (13)$$

419 The gradually changing correlations underlying these datasets allow us to evaluate the recovery of dynamic  
420 correlations when each timepoint’s correlation matrix is unique (as in the random datasets), but where the  
421 correlation dynamics are structured and exhibit first-order autocorrelations (as in the constant datasets).

422 **Event.** We generated a fourth set of 100 synthetic datasets whose underlying correlation matrices exhibited  
423 prolonged intervals of stability, interspersed with abrupt changes. For each dataset, we used Equation 11  
424 to generate 5 random covariance matrices. We constructed a timeseries where each set of 60 consecutive  
425 samples was drawn from a Gaussian with the same covariance matrix. These datasets were intended to  
426 simulate a system that exhibits periods of stability punctuated by occasional abrupt state changes.

#### 427 Synthetic data: simulating dynamic high-order correlations

428 We developed an iterative procedure for constructing timeseries data that exhibits known dynamic high-  
429 order correlations. The procedure builds on our approach to generating dynamic first-order correlations.  
430 Essentially, once we generate a timeseries with known first-order correlations, we can use the known first-  
431 order correlations as a template to generate a new timeseries of second-order correlations. In turn, we can  
432 generate a timeseries of third-order correlations from the second-order correlations, and so on. In general,  
433 we can generate order  $n$  correlations given a timeseries of order  $n - 1$  correlations, for any  $n > 1$ . Finally,

434 given the order  $n$  timeseries, we can reverse the preceding process to generate an order  $n - 1$  timeseries, an  
435 order  $n - 2$  order timeseries, and so on, until we obtain an order 0 timeseries of simulated data that reflects  
436 the chosen high-order dynamics.

437 The central mathematical operation in our procedure is the Kronecker product ( $\otimes$ ). The Kronecker  
438 product of a  $K \times K$  matrix,  $m_1$ , with itself (i.e.,  $m_1 \otimes m_1$ ) produces a new  $K^2 \times K^2$  matrix,  $m_2$  whose entries  
439 reflect a scaled tiling of the entries in  $m_1$ . If these tilings (scaled copies of  $m_1$ ) are indexed by row and column,  
440 then the tile in the  $i^{\text{th}}$  row and  $j^{\text{th}}$  column contains the entries of  $m_1$ , multiplied by  $m_1(i, j)$ . Following this  
441 pattern, the Kronecker product  $m_2 \otimes m_2$  yields the  $K^4 \times K^4$  matrix  $m_3$  whose tiles are scaled copies of  $m_2$ . In  
442 general, repeated applications of the Kronecker self-product may be used to generate  $m_{n+1} = m_n \otimes m_n$  for  
443  $n > 1$ , where  $m_{n+1}$  is a  $K^{2^n} \times K^{2^n}$  matrix. After generating a first-order timeseries of dynamic correlations (see  
444 Synthetic data: simulating dynamic first-order correlations), we use this procedure (applied independently  
445 at each timepoint) to transform it into a timeseries of  $n^{\text{th}}$ -order correlations. When  $m_{n+1}$  is generated in this  
446 way, the temporal structure of the full timeseries (i.e., constant, random, ramping, event) is preserved, since  
447 changes in the original first-order timeseries are also reflected in the scaled tilings of itself that comprise the  
448 higher-order matrices.

449 Given a timeseries of  $n^{\text{th}}$ -order correlations, we then need to work “backwards” in order to generate the  
450 order-zero timeseries. If the  $n^{\text{th}}$ -order correlation matrix at a given timepoint is  $m_n$ , then we can generate an  
451 order  $n - 1$  correlation matrix (for  $n > 1$ ) by taking a draw from  $\mathcal{N}(0, m_n)$  and reshaping the resulting vector  
452 to have square dimensions. To force the resulting matrix to be symmetric, we remove its lower triangle, and  
453 replace the lower triangle with (a reflected version of) its upper triangle. Intuitively, the re-shaped matrix  
454 will look like a noisy (but symmetric) version of the template matrix,  $m_{n-1}$ . (When  $n = 1$ , no re-shaping  
455 is needed; the resulting  $K$ -dimensional vector may be used as the observation at the given timepoint.)  
456 After independently drawing each timepoint’s order  $n - 1$  correlation matrix from that timepoint’s order  
457  $n$  correlation matrix, this process can be applied repeatedly until  $n = 0$ . This results in a  $K$ -dimensional  
458 timeseries of  $T$  observations containing the specified high-order correlations at orders 1 through  $n$ . Following  
459 our approach to generating synthetic data exhibiting known first-order correlations, we constructed a total  
460 of 400 additional multivariate timeseries, collectively reflecting a total of 4 qualitatively different patterns of  
461 dynamic correlations (i.e., 100 datasets reflecting each type of dynamic pattern: constant, random, ramping,  
462 and event). Each timeseries comprised 10 zero-order features (dimensions) that varied over 300 timepoints.  
463 After applying our dynamic correlation estimation procedure, this yielded a 100-dimensional timeseries of  
464 first-order features that could then be used to estimate dynamic second-order correlations. (We chose to  
465 use  $K = 10$  zero-order features for our higher order simulations in order to put the accuracy computations  
466 displayed in Figs. 2 and 3 on a roughly even footing.)

467 **Functional neuroimaging data collected during story listening**

468 We examined an fMRI dataset collected by<sup>36</sup> that the authors have made publicly available at [arks.princeton.edu/ark:/88435/ds](https://arks.princeton.edu/ark:/88435/ds)  
469 The dataset comprises neuroimaging data collected as participants listened to an audio recording of a story  
470 (intact condition; 36 participants), listened to temporally scrambled recordings of the same story (17 partici-  
471 pants in the paragraph-scrambled condition listened to the paragraphs in a randomized order and 36 in the  
472 word-scrambled condition listened to the words in a randomized order), or lay resting with their eyes open  
473 in the scanner (rest condition; 36 participants). Full neuroimaging details may be found in the original paper  
474 for which the data were collected<sup>36</sup>. Procedures were approved by the Princeton University Committee on  
475 Activities Involving Human Subjects, and by the Western Institutional Review Board (Puyallup, WA). All  
476 subjects were native English speakers with normal hearing and provided written informed consent.

477 **Hierarchical topographic factor analysis (HTFA).** Following our prior related work, we used HTFA<sup>11</sup>  
478 to derive a compact representation of the neuroimaging data. In brief, this approach approximates the  
479 timeseries of voxel activations (44,415 voxels) using a much smaller number of radial basis function (RBF)  
480 nodes (in this case, 700 nodes, as determined by an optimization procedure<sup>11</sup>). This provides a convenient  
481 representation for examining full-brain network dynamics. All of the analyses we carried out on the  
482 neuroimaging dataset were performed in this lower-dimensional space. In other words, each participant's  
483 data matrix,  $X_0$ , was a number-of-timepoints by 700 matrix of HTFA-derived factor weights (where the row  
484 and column labels were matched across participants). Code for carrying out HTFA on fMRI data may be  
485 found as part of the BrainIAK toolbox<sup>88</sup>, which may be downloaded at [brainiak.org](http://brainiak.org).

486 **Temporal decoding**

487 We sought to identify neural patterns that reflected participants' ongoing cognitive processing of incoming  
488 stimulus information. As reviewed by<sup>36</sup>, one way of homing in on these stimulus-driven neural patterns is  
489 to compare activity patterns across individuals (e.g., using ISFC analyses). In particular, neural patterns will  
490 be similar across individuals to the extent that the neural patterns under consideration are stimulus-driven,  
491 and to the extent that the corresponding cognitive representations are reflected in similar spatial patterns  
492 across people<sup>55</sup>. Following this logic, we used an across-participant temporal decoding test developed  
493 by<sup>11</sup> to assess the degree to which different neural patterns reflected ongoing stimulus-driven cognitive  
494 processing across people (Fig. 10). The approach entails using a subset of the data to train a classifier to  
495 decode stimulus timepoints (i.e., moments in the story participants listened to) from neural patterns. We  
496 use decoding (forward inference) accuracy on held-out data, from held-out participants, as a proxy for the

497 extent to which the inputted neural patterns reflected stimulus-driven cognitive processing in a similar way  
498 across individuals.

499 **Forward inference and decoding accuracy**

500 We used an across-participant correlation-based classifier to decode which stimulus timepoint matched  
501 each timepoint's neural pattern (Fig. 10). We first divided the participants into two groups: a template group,  
502  $\mathcal{G}_{\text{template}}$  (i.e., training data), and a to-be-decoded group,  $\mathcal{G}_{\text{decode}}$  (i.e., test data). We used Equation 7 to  
503 compute a DISFC matrix for each group ( $\bar{\mathbf{C}}_{\text{template}}$  and  $\bar{\mathbf{C}}_{\text{decode}}$ , respectively). We then correlated the rows of  
504  $\bar{\mathbf{C}}_{\text{template}}$  and  $\bar{\mathbf{C}}_{\text{decode}}$  to form a number-of-timepoints by number-of-timepoints decoding matrix,  $\Lambda$ . In this  
505 way, the rows of  $\Lambda$  reflected timepoints from the template group, while the columns reflected timepoints  
506 from the to-be-decoded group. We used  $\Lambda$  to assign temporal labels to each row  $\bar{\mathbf{C}}_{\text{decode}}$  using the row of  
507  $\bar{\mathbf{C}}_{\text{template}}$  with which it was most highly correlated. We then repeated this decoding procedure, but using  
508  $\mathcal{G}_{\text{decode}}$  as the template group and  $\mathcal{G}_{\text{template}}$  as the to-be-decoded group. Given the true timepoint labels (for  
509 each group), we defined the decoding accuracy as the average proportion of correctly decoded timepoints,  
510 across both groups. We defined the relative decoding accuracy as the difference between the decoding  
511 accuracy and chance accuracy (i.e.,  $\frac{1}{T}$ ).

512 **Feature weighting and testing**

513 We sought to examine which types of neural features (i.e., activations, first-order dynamic correlations, and  
514 higher-order dynamic correlations) were informative to the temporal decoders. Using the notation above,  
515 these features correspond to  $\mathbf{X}_0, \mathbf{X}_1, \mathbf{X}_2, \mathbf{X}_3$ , and so on.

516 [Figure 10 about here.]

517 One challenge to fairly evaluating high-order correlations is that if the kernel used in Equation 4 is  
518 wider than a single timepoint, each repeated application of the equation will result in further temporal  
519 blur. Because our primary assessment metric is temporal decoding accuracy, this unfairly biases against  
520 detecting meaningful signal in higher-order correlations (relative to lower-order correlations). We attempted  
521 to mitigate temporal blur in estimating each  $\mathbf{X}_n$  by using a Dirac  $\delta$  function kernel (which places all of its  
522 mass over a single timepoint; Fig. 9b, 10a) to compute each lower-order correlation ( $\mathbf{X}_1, \mathbf{X}_2, \dots, \mathbf{X}_{n-1}$ ). We  
523 then used a new (potentially wider, as described below) kernel to compute  $\mathbf{X}_n$  from  $\mathbf{X}_{n-1}$ . In this way,  
524 temporal blurring was applied only in the last step of computing  $\mathbf{X}_n$ . We note that, because each  $\mathbf{X}_n$  is a  
525 low-dimensional representation of the corresponding  $\mathbf{Y}_n$ , the higher-order correlations we estimated reflect  
526 true correlations in the data with lower-fidelity than estimates of lower-order correlations. Therefore, even

527 after correcting for temporal blurring, our approach is still biased against finding meaningful signal in  
528 higher-order correlations.

529 After computing each  $\mathbf{X}_1, \mathbf{X}_2, \dots, \mathbf{X}_{n-1}$  for each participant, we divided participants into two equally sized  
530 groups ( $\pm 1$  for odd numbers of participants):  $\mathcal{G}_{\text{train}}$  and  $\mathcal{G}_{\text{test}}$ . We then further subdivided  $\mathcal{G}_{\text{train}}$  into  $\mathcal{G}_{\text{train}_1}$   
531 and  $\mathcal{G}_{\text{train}_2}$ . We then computed  $\Lambda$  (temporal correlation) matrices for each type of neural feature, using  $\mathcal{G}_{\text{train}_1}$   
532 and  $\mathcal{G}_{\text{train}_2}$ . This resulted in  $n + 1$   $\Lambda$  matrices (one for the original timeseries of neural activations, and one  
533 for each of  $n$  orders of dynamic correlations). Our objective was to find a set of weights for each of these  
534  $\Lambda$  matrices such that the weighted average of the  $n + 1$  matrices yielded the highest decoding accuracy.  
535 We used quasi-Newton gradient ascent<sup>89</sup>, using decoding accuracy (for  $\mathcal{G}_{\text{train}_1}$  and  $\mathcal{G}_{\text{train}_2}$ ) as the objective  
536 function to be maximized, to find an optimal set of training data-derived weights,  $\phi_{0,1,\dots,n}$ , where  $\sum_{i=0}^n \phi_i = 1$   
537 and where  $\phi_i \geq 0 \forall i \in [0, 1, \dots, n]$ .

538 After estimating an optimal set of weights, we computed a new set of  $n + 1$   $\Lambda$  matrices correlating the  
539 DISFC patterns from  $\mathcal{G}_{\text{train}}$  and  $\mathcal{G}_{\text{test}}$  at each timepoint. We use the resulting decoding accuracy of  $\mathcal{G}_{\text{test}}$   
540 timepoints (using the weights in  $\phi_{0,1,\dots,n}$  to average the  $\Lambda$  matrices) to estimate how informative the set of  
541 neural features containing up to  $n^{\text{th}}$  order correlations were.

542 We used a permutation-based procedure to form stable estimates of decoding accuracy for each set of  
543 neural features. In particular, we computed the decoding accuracy for each of 10 random group assignments  
544 of  $\mathcal{G}_{\text{train}}$  and  $\mathcal{G}_{\text{test}}$ . We report the mean accuracy (along with 95% confidence intervals) for each set of neural  
545 features.

#### 546 Identifying robust decoding results

547 The temporal decoding procedure we use to estimate which neural features support ongoing cognitive  
548 processing is governed by several parameters. In particular, Equation 4 requires defining a kernel function,  
549 which can take on different shapes and widths. For a fixed set of neural features, each of these parameters  
550 can yield different decoding accuracies. Further, the best decoding accuracy for a given timepoint may be  
551 reliably achieved by one set of parameters, whereas the best decoding accuracy for another timepoint might  
552 be reliably achieved by a different set of parameters, and the best decoding accuracy across all timepoints  
553 might be reliably achieved by still another different set of parameters. Rather than attempting to maximize  
554 decoding accuracy, we sought to discover the trends in the data that were robust to classifier parameters  
555 choices. Specifically, we sought to characterize how decoding accuracy varied (under different experimental  
556 conditions) as a function of which neural features were considered.

557 To identify decoding results that were robust to specific classifier parameter choices, we repeated our

558 decoding analyses after substituting into Equation 4 each of a variety of kernel shapes and widths. We  
559 examined Gaussian (Fig. 9c), Laplace (Fig. 9d), and Mexican Hat (Fig. 9e) kernels, each with widths of 5, 10,  
560 20, and 50 samples. We then report the average decoding accuracies across all of these parameter choices.  
561 This enabled us to (partially) factor out performance characteristics that were parameter-dependent, within  
562 the set of parameters we examined.

563 **Reverse inference**

564 The dynamic patterns we examined comprise high-dimensional correlation patterns at each timepoint. To  
565 help interpret the resulting patterns in the context of other studies, we created summary maps by computing  
566 the across-timepoint average pairwise correlations at each order of analysis (first order, second order, etc.).  
567 We selected the 10 strongest (absolute value) correlations at each order. Each correlation is between the  
568 dynamic activity patterns (or patterns of dynamic high-order correlations) measured at two RBF nodes (see  
569 Hierarchical Topographic Factor Analysis). Therefore, the 10 strongest correlations involved up to 20 RBF  
570 nodes. Each RBF defines a spatial function whose activations range from 0 to 1. We constructed a map  
571 of RBF components that denoted the endpoints of the 10 strongest correlations (we set each RBF to have a  
572 maximum value of 1). We then carried out a meta analysis using Neurosynth<sup>38</sup> to identify the 10 terms most  
573 commonly associated with the given map. This resulted in a set of 10 terms associated with the average  
574 dynamic correlation patterns at each order.

575 **Data Availability**

576 The authors declare that the data supporting the findings of this study as well as the source data for  
577 this paper are available at [github.com/ContextLab/timecorr-paper/releases/tag/v0.4](https://github.com/ContextLab/timecorr-paper/releases/tag/v0.4) and has been deposited  
578 in the Zenodo database under accession code <https://doi.org/10.5281/zenodo.5165253>. The source data  
579 underlying Figs. 2-6 and Supplementary Figs. S1-S9 are provided as a Source Data file. Source Data  
580 are provided with the manuscript. The raw fMRI data are protected and are not available due to  
581 data privacy laws. The processed fMRI dataset collected by<sup>36</sup> has been made publicly available<sup>91</sup> at  
582 [arks.princeton.edu/ark:/88435/dsp015d86p269k](https://arks.princeton.edu/ark:/88435/dsp015d86p269k).

583 **Code Availability**

584 All of our analysis code may be downloaded from [github.com/ContextLab/timecorr-paper/releases/tag/v0.4](https://github.com/ContextLab/timecorr-paper/releases/tag/v0.4).  
585 We have also published a companion Python toolbox that may be downloaded from [timecorr.readthedocs.io](https://timecorr.readthedocs.io).

586 **Acknowledgements**

587 We acknowledge discussions with Luke Chang, Vassiki Chauhan, Hany Farid, Paxton Fitzpatrick, Andrew  
588 Heusser, Eshin Jolly, Aaron Lee, Qiang Liu, Matthijs van der Meer, Judith Mildner, Gina Notaro, Stephen  
589 Satterthwaite, Emily Whitaker, Weizhen Xie, and Kirsten Ziman. Our work was supported in part by NSF  
590 EPSCoR Award Number 1632738 to J.R.M. and by a sub-award of DARPA RAM Cooperative Agreement  
591 N66001-14-2-4-032 to J.R.M. The content is solely the responsibility of the authors and does not necessarily  
592 represent the official views of our supporting organizations.

593 **Author contributions**

594 Concept: J.R.M. Implementation: T.H.C., L.L.W.O., and J.R.M. Analyses: L.L.W.O. and J.R.M. Writing:  
595 L.L.W.O. and J.R.M.

596 **Competing interests**

597 The authors declare no competing interests.

598 **References**

- 599 [1] Haxby, J. V. *et al.* Distributed and overlapping representations of faces and objects in ventral temporal  
600 cortex. *Science* **293**, 2425–2430 (2001).
- 601 [2] Norman, K. A., Polyn, S. M., Detre, G. J. & Haxby, J. V. Beyond mind-reading: multi-voxel pattern  
602 analysis of fMRI data. *Trends in Cognitive Sciences* **10**, 424–430 (2006).
- 603 [3] Tong, F. & Pratte, M. S. Decoding patterns of human brain activity. *Annual Review of Psychology* **63**,  
604 483–509 (2012).
- 605 [4] Mitchell, T. M. *et al.* Predicting human brain activity associated with the meanings of nouns. *Science*  
606 **320**, 1191 (2008).
- 607 [5] Kamitani, Y. & Tong, F. Decoding the visual and subjective contents of the human brain. *Nature  
608 Neuroscience* **8**, 679–685 (2005).
- 609 [6] Nishimoto, S. *et al.* Reconstructing visual experience from brain activity evoked by natural movies.  
610 *Current Biology* **21**, 1–6 (2011).

- 611 [7] Pereira, F. *et al.* Toward a universal decoder of linguistic meaning from brain activation. *Nature*  
612 *Communications* **9**, 1–13 (2018).
- 613 [8] Huth, A. G., Nisimoto, S., Vu, A. T. & Gallant, J. L. A continuous semantic space describes the  
614 representation of thousands of object and action categories across the human brain. *Neuron* **76**, 1210–  
615 1224 (2012).
- 616 [9] Huth, A. G., de Heer, W. A., Griffiths, T. L., Theunissen, F. E. & Gallant, J. L. Natural speech reveals the  
617 semantic maps that tile human cerebral cortex. *Nature* **532**, 453–458 (2016).
- 618 [10] Etzel, J. A., Gazzola, V. & Keysers, C. An introduction to anatomical ROI-based fMRI classification.  
619 *Brain Research* **1281**, 114–125 (2009).
- 620 [11] Manning, J. R. *et al.* A probabilistic approach to discovering dynamic full-brain functional connectivity  
621 patterns. *NeuroImage* **180**, 243–252 (2018).
- 622 [12] Fong, A. H. C. *et al.* Dynamic functional connectivity during task performance and rest predicts  
623 individual differences in attention across studies. *NeuroImage* **188**, 14–25 (2019).
- 624 [13] Grossberg, S. Nonlinear neural networks: principles, mechanisms, and architectures. *Neural Networks*  
625 **1**, 17–61 (1988).
- 626 [14] Friston, K. J. The labile brain. I. neuronal transients and nonlinear coupling. *Philosophical Transactions  
627 of the Royal Society of London* **355B**, 215–236 (2000).
- 628 [15] Sporns, O. & Honey, C. J. Small worlds inside big brains. *Proceedings of the National Academy of Sciences,  
629 USA* **103**, 19219–19220 (2006).
- 630 [16] Bassett, D., Meyer-Lindenberg, A., Achard, S., Duke, T. & Bullmore, E. Adaptive reconfiguration of  
631 fractal small-world human brain functional networks. *Proceedings of the National Academy of Sciences,  
632 USA* **103**, 19518–19523 (2006).
- 633 [17] Turk-Browne, N. B. Functional interactions as big data in the human brain. *Science* **342**, 580–584 (2013).
- 634 [18] Demertzi, A. *et al.* Human consciousness is supported by dynamic complex patterns of brain signal  
635 coordination. *Science Advances* **5**, eaat7603 (2019).
- 636 [19] Solomon, S. H., Medaglia, J. D. & Thompson-Schill, S. L. Implementing a concept network model.  
637 *Behavior Research Methods* **51**, 1717–1736 (2019).

- 638 [20] Lurie, D. *et al.* On the nature of time-varying functional connectivity in resting fMRI. *PsyArXiv*  
639 [doi.org/10.31234/osf.io/xtzre](https://doi.org/10.31234/osf.io/xtzre) (2018).
- 640 [21] Preti, M. G., Bolton, T. A. W. & Van De Ville, D. The dynamic functional connectome: state-of-the-art  
641 and perspectives. *NeuroImage* **160**, 41–54 (2017).
- 642 [22] Zou, Y., Donner, R. V., Marwan, N., Donges, J. F. & Kurths, J. Complex network approaches to nonlinear  
643 time series analysis. *Physics Reports* **787**, 1–97 (2019).
- 644 [23] Mack, M. L., Preston, A. R. & Love, B. C. Medial prefrontal cortex compresses concept representations  
645 through learning. *bioRxiv* [doi.org/10.1101/178145](https://doi.org/10.1101/178145) (2017).
- 646 [24] Bressler, S. L. & Kelso, J. A. S. Cortical coordination dynamics and cognition. *Trends in Cognitive Sciences*  
647 **5**, 26–36 (2001).
- 648 [25] McIntosh, A. R. Towards a network theory of cognition. *Neural Networks* **13**, 861–870 (2000).
- 649 [26] Reimann, M. W. *et al.* Cliques of neurons bound into cavities provide a missing link between structure  
650 and function. *Frontiers in Computational Neuroscience* **11**, 1–16 (2017).
- 651 [27] Beaty, R. E., Benedek, M., Silvia, P. J. & Schacter, D. L. Creative cognition and brain network dynamics.  
652 *Trends in Cognitive Sciences* **20**, 87–95 (2016).
- 653 [28] Bullmore, E. & Sporns, O. Complex brain networks: graph theoretical analysis of structural and  
654 functional systems. *Nature Reviews Neuroscience* **10**, 186–198 (2009).
- 655 [29] Pearson, K. On lines and planes of closest fit to systems of points in space. *The London, Edinburgh, and*  
656 *Dublin Philosophical Magazine and Journal of Science* **2**, 559–572 (1901).
- 657 [30] McIntosh, A. R. & Jirsa, V. K. The hidden repertoire of brain dynamics and dysfunction. *Network*  
658 *Neuroscience* [doi.org/10.1162/netn\\_a\\_00107](https://doi.org/10.1162/netn_a_00107) (2019).
- 659 [31] Toker, D. & Sommer, F. T. Information integration in large brain networks. *PLoS Computational Biology*  
660 **15**, e1006807 (2019).
- 661 [32] Gonzalez-Castillo, J. *et al.* Imaging the spontaneous flow of thought: distinct periods of cognition  
662 contribute to dynamic functional connectivity during rest. *NeuroImage* **202** (2019).
- 663 [33] Landau, E. Zur relativen Wertbemessung der Turnierresultate. *Deutsches Wochenschach* **11**, 366–369  
664 (1895).

- 665 [34] Betzel, R. F., Byrge, L., Esfahlani, F. Z. & Kennedy, D. P. Temporal fluctuations in the brain's modular  
666 architecture during movie-watching. *bioRxiv* doi.org/10.1101/750919 (2019).
- 667 [35] Sizemore, A. E. *et al.* Cliques and cavities in the human connectome. *Journal of Computational Neuroscience*  
668 **44**, 115–145 (2018).
- 669 [36] Simony, E., Honey, C. J., Chen, J. & Hasson, U. Dynamic reconfiguration of the default mode network  
670 during narrative comprehension. *Nature Communications* **7**, 1–13 (2016).
- 671 [37] Hasson, U., Yang, E., Vallines, I., Heeger, D. J. & Rubin, N. A hierarchy of temporal receptive windows  
672 in human cortex. *The Journal of Neuroscience* **28**, 2539–2550 (2008).
- 673 [38] Rubin, T. N. *et al.* Decoding brain activity using a large-scale probabilistic functional-anatomical atlas  
674 of human cognition. *PLoS Computational Biology* **13**, e1005649 (2017).
- 675 [39] Park, H.-J., Friston, K. J., Pae, C., Park, B. & Razi, A. Dynamic effective connectivity in resting state  
676 fMRI. *NeuroImage* **180**, 594–608 (2018).
- 677 [40] Roy, D. S. *et al.* Brain-wide mapping of contextual fear memory engram ensembles supports the  
678 dispersed engram complex hypothesis. *bioRxiv* doi.org/10.1101/668483 (2019).
- 679 [41] Liégeois, R. *et al.* Resting brain dynamics at different timescales capture distinct aspects of human  
680 behavior. *Nature Communications* **10**, 1–9 (2019).
- 681 [42] Chang, C. & Glover, G. H. Time-frequency dynamics of resting-state brain connectivity measured with  
682 fMRI. *NeuroImage* **50**, 81–98 (2010).
- 683 [43] Zheng, M., Allard, A., Hagmann, P. & Serrano, M. . . A. Geometric renormalization unravels self-  
684 similarity of the multiscale human connectome. *arXiv* 1904.11793 (2019).
- 685 [44] Baldassano, C. *et al.* Discovering event structure in continuous narrative perception and memory.  
686 *Neuron* **95**, 709–721 (2017).
- 687 [45] Hasson, U., Chen, J. & Honey, C. J. Hierarchical process memory: memory as an integral component  
688 of information processing. *Trends in Cognitive Sciences* **19**, 304–315 (2015).
- 689 [46] Honey, C. J. *et al.* Slow cortical dynamics and the accumulation of information over long timescales.  
690 *Neuron* **76**, 423–434 (2012).
- 691 [47] Lerner, Y., Honey, C. J., Silbert, L. J. & Hasson, U. Topographic mapping of a hierarchy of temporal  
692 receptive windows using a narrated story. *The Journal of Neuroscience* **31**, 2906–2915 (2011).

- 693 [48] Lerner, Y., Honey, C. J., Katkov, M. & Hasson, U. Temporal scaling of neural responses to compressed  
694 and dilated natural speech. *Journal of Neurophysiology* **111**, 2433–2444 (2014).
- 695 [49] Chien, H.-Y. S. & Honey, C. J. Constructing and forgetting temporal context in the human cerebral  
696 cortex. *bioRxiv* [doi.org/10.1101/761593](https://doi.org/10.1101/761593) (2019).
- 697 [50] Lee, C. S., Aly, M. & Baldassano, C. Anticipation of temporally structured events in the brain. *bioRxiv*  
698 [10.1101/2020.10.14.338145](https://doi.org/10.1101/2020.10.14.338145) (2020).
- 699 [51] Fallon, J., Ward, P. G. D., Parkes, L. & Oldham, S. Timescales of spontaneous fMRI fluctuations relate  
700 to structural connectivity in the brain. *Network Neuroscience* **4**, 788–806 (2020).
- 701 [52] Shappell, H., Caffo, B. S., Pekar, J. J. & Lindquist, M. A. Improved state change estimation in dynamic  
702 functional connectivity using hidden semi-Markov models. *NeuroImage* **191**, 243–257 (2019).
- 703 [53] Vidaurre, D. *et al.* Discovering dynamic brain networks from big data in rest and task. *NeuroImage* **180**,  
704 646–656 (2018).
- 705 [54] Allen, E. A. *et al.* Tracking whole-brain connectivity dynamics in the resting state. *Cerebral Cortex* **24**,  
706 663–676 (2012).
- 707 [55] Simony, E. & Chang, C. Analysis of stimulus-induced brain dynamics during naturalistic paradigms.  
708 *NeuroImage* **216**, 116461 (2020).
- 709 [56] Zar, J. H. *Biostatistical analysis* (Prentice-Hall, 2010).
- 710 [57] Tipping, M. E. & Bishop, C. M. Probabilistic principal component analysis. *Journal of Royal Statistical  
711 Society, Series B* **61**, 611–622 (1999).
- 712 [58] Spearman, C. General intelligence, objectively determined and measured. *American Journal of Psychology*  
713 **15**, 201–292 (1904).
- 714 [59] Jutten, C. & Herault, J. Blind separation of sources, part I: an adaptive algorithm based on neuromimetic  
715 architecture. *Signal Processing* **24**, 1–10 (1991).
- 716 [60] Comon, P., Jutten, C. & Herault, J. Blind separation of sources, part II: problems statement. *Signal  
717 Processing* **24**, 11–20 (1991).
- 718 [61] van der Maaten, L. J. P. & Hinton, G. E. Visualizing high-dimensional data using t-SNE. *Journal of  
719 Machine Learning Research* **9**, 2579–2605 (2008).

- 720 [62] McInnes, L., Healy, J. & Melville, J. UMAP: uniform manifold approximation and projection for  
721 dimension reduction. *arXiv* **1802** (2018).
- 722 [63] Lee, D. D. & Seung, H. S. Learning the parts of objects by non-negative matrix factorization. *Nature*  
723 **401**, 788–791 (1999).
- 724 [64] Manning, J. R., Ranganath, R., Norman, K. A. & Blei, D. M. Topographic factor analysis: a Bayesian  
725 model for inferring brain networks from neural data. *PLoS One* **9**, e94914 (2014).
- 726 [65] Gershman, S. J., Blei, D. M., Pereira, F. & Norman, K. A. A topographic latent source model for fMRI  
727 data. *NeuroImage* **57**, 89–100 (2011).
- 728 [66] Mairal, J. B., Bach, F., Ponce, J. & Sapiro, G. Online dictionary learning for sparse coding. *Proceedings*  
729 *of the International Conference on Machine Learning* 689–696 (2009).
- 730 [67] Mairal, J., Ponce, J., Sapiro, G., Zisserman, A. & Bach, F. R. Supervised dictionary learning. *Advances*  
731 *in Neural Information Processing Systems* 1033–1040 (2009).
- 732 [68] Hinton, G. E. & Salakhutdinov, R. R. Reducing the dimensionality of data with neural networks. *Science*  
733 **313**, 504–507 (2006).
- 734 [69] Newman, M. E. J. A measure of betweenness centrality based on random walks. *Social Networks* **27**,  
735 39–54 (2005).
- 736 [70] Opsahl, T., Agneessens, F. & Skvoretz, J. Node centrality in weighted networks: generalizing degree  
737 and shortest paths. *Social Networks* **32**, 245–251 (2010).
- 738 [71] Barthélemy, M. Betweenness centrality in large complex networks. *European Physical Journal B* **38**,  
739 163–168 (2004).
- 740 [72] Geisberger, R., Sanders, P. & Schultes, D. Better approximation of betweenness centrality. *Proceedings*  
741 *of the Meeting on Algorithm Engineering and Experiments* 90–100 (2008).
- 742 [73] Freeman, L. C. A set of measures of centrality based on betweenness. *Sociometry* **40**, 35–41 (1977).
- 743 [74] Rao, C. R. Diversity and dissimilarity coefficients: a unified approach. *Theoretical Population Biology* **21**,  
744 24–43 (1982).
- 745 [75] Lin, J. Divergence measures based on the Shannon entropy. *IEEE Transactions on Information Theory* **37**,  
746 145–151 (2009).

- 747 [76] Ricotta, C. & Szeidl, L. Towards a unifying approach to diversity measures: bridging the gap between  
748 the Shannon entropy and Rao's quadratic index. *Theoretical Population Biology* **70**, 237–243 (2006).
- 749 [77] Newman, M. E. J. The mathematics of networks. *The New Palgrave Encyclopedia of Economics* **2**, 1–12  
750 (2008).
- 751 [78] Bonacich, P. Some unique properties of eigenvector centrality. *Social Networks* **29**, 555–564 (2007).
- 752 [79] Lohmann, G. *et al.* Eigenvector centrality mapping for analyzing connectivity patterns in fMRI data of  
753 the human brain. *PLoS One* **5**, e10232 (2010).
- 754 [80] Halu, A., Mondragón, R. J., Panzarasa, P. & Bianconi, G. Multiplex PageRank. *PLoS One* **8**, e78293  
755 (2013).
- 756 [81] Honey, C. J., Kötter, R., Breakspear, M. & Sporns, O. Network structure of cerebral cortex shapes  
757 functional connectivity on multiple time scales. *Proceedings of the National Academy of Sciences, USA* **104**,  
758 10240–10245 (2007).
- 759 [82] Schreiber, T. Measuring information transfer. *Physical Review Letters* **85**, 461–464 (2000).
- 760 [83] Alvarez-Hamelin, I., Dall'Asta, L., Barrat, A. & Vespignani, A. *k*-corr decomposition: a tool for the  
761 visualiztion of large scale networks. *arXiv cs/0504107v2* (2005).
- 762 [84] Christakis, N. A. & Fowler, J. H. Social network sensors for early detection of contagious outbreaks.  
763 *PLoS One* **5**, e12948 (2010).
- 764 [85] Rubinov, M. & Sporns, O. Complex network measures of brain connectivity: uses and interpretations.  
765 *NeuroImage* **52**, 1059–1069 (2010).
- 766 [86] Estrada, E. & Rodríguez-Velázquez, J. A. Subgraph centrality in complex networks. *Physical Review E*  
767 **71**, 056103 (2005).
- 768 [87] Thompson, W. H., Richter, C. G., Plavén-Sigray, P. & Fransson, P. Simulations to benchmark time-  
769 varying connectivity methods for fMRI. *PLoS Computational Biology* **14**, e1006196 (2018).
- 770 [88] Capota, M. *et al.* Brain imaging analysis kit (2017).
- 771 [89] Nocedal, J. & Wright, S. J. *Numerical optimization* (Springer, New York, NY, 2006).
- 772 [90] Combrisson, E. *et al.* Visbrain: a multi-purpose GPU-accelerated open-source suite for multimodal  
773 brain data visualization. *Frontiers in Neuroinformatics* **13**, 1–14 (2019).

<sup>774</sup> [91] Simony, E., Honey, C. J., Chen, J. & Hasson, U. Dynamic reconfiguration of the default mode network  
<sup>775</sup> during narrative comprehension. *DataSpace* <http://arks.princeton.edu/ark:/88435/dsp015d86p269k>  
<sup>776</sup> (2016).

*777* **Figures**

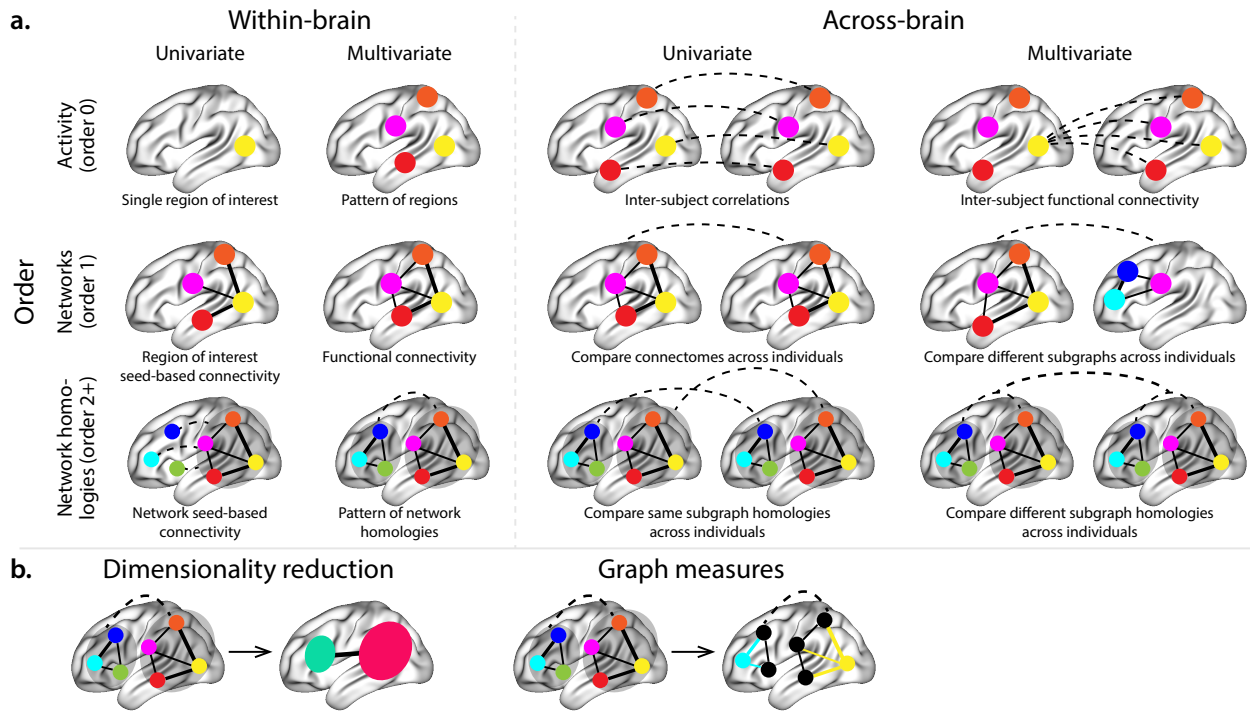


**Figure 1: Neural patterns. a. A space of neural features.** Within-brain analyses are carried out within a single brain, whereas across-brain analyses compare neural patterns across two or more individuals' brains. Univariate analyses characterize the activities of individual units (e.g., nodes, small networks, hierarchies of networks, etc.), whereas multivariate analyses characterize the patterns of activity across units. Order 0 patterns involve individual nodes; order 1 patterns involve node-node interactions; order 2 (and higher) patterns relate to interactions between homologous networks. Each of these patterns may be static (e.g., averaging over time) or dynamic. **b. Summarizing neural patterns.** To efficiently compute with complex neural patterns, it can be useful to characterize the patterns using summary measures. Dimensionality reduction algorithms project the patterns onto lower-dimensional spaces whose dimensions reflect weighted combinations or non-linear transformations of the dimensions in the original space. Graph measures characterize each unit's participation in its associated network.

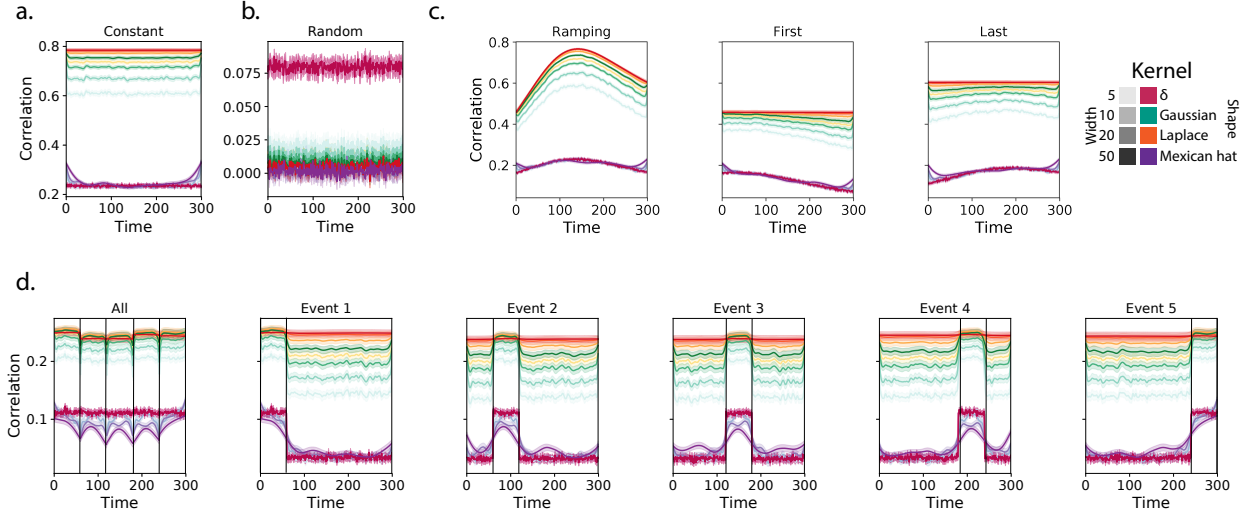


**Figure 2: Recovering known dynamic first-order correlations from synthetic data.** Each panel displays the average correlations between the vectorized upper triangles of the recovered correlation matrix at each timepoint and either the true underlying correlation at each timepoint or a reference correlation matrix. (The averages are taken across 100 different randomly generated synthetic datasets of each given category, each with  $K = 50$  features and  $T = 300$  timepoints.) Error ribbons denote 95% confidence intervals of the mean (taken across datasets). Different colors denote different kernel shapes, and the shading within each color family denotes the kernel width parameter. For a complete description of each synthetic dataset, see Synthetic data: simulating dynamic first-order correlations. **a. Constant correlations.** These datasets have a stable (unchanging) underlying correlation matrix. **b. Random correlations.** These datasets are generated using a new independently drawn correlation matrix at each new timepoint. **c. Ramping correlations.** These datasets are generated by smoothly varying the underlying correlations between the randomly drawn correlation matrices at the first and last timepoints. The left panel displays the correlations between the recovered dynamic correlations and the underlying ground truth correlations. The middle panel compares the recovered correlations with the first timepoint's correlation matrix. The right panel compares the recovered correlations with the last timepoint's correlation matrix. **d. Event-based correlations.** These datasets are each generated using five randomly drawn correlation matrices that each remain stable for a fifth of the total timecourse. The left panel displays the correlations between the recovered dynamic correlations and the underlying ground truth correlations. The right panels compare the recovered correlations with the correlation matrices unique to each event. The vertical lines denote event boundaries. Source data are provided as a Source Data file.

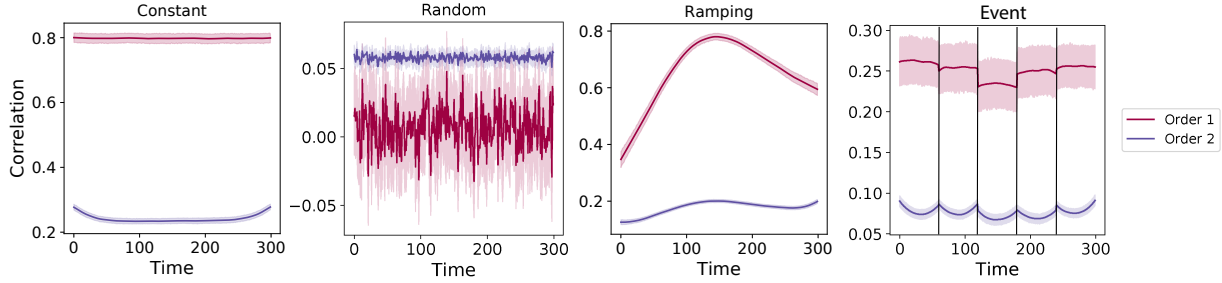


**Figure 3: Recovery of simulated first-order and second-order dynamic correlations.** Each panel displays the average correlations between the vectorized upper triangles of the recovered first-order and second-order correlation matrices and the true (simulated) first-order and second order correlation matrices at each timepoint and for each synthetic dataset. (The averages are taken across 100 different randomly generated synthetic datasets of each given category, each with  $K = 10$  features and  $T = 300$  timepoints.) Error ribbons denote 95% confidence intervals of the mean (taken across datasets). For a complete description of each synthetic dataset, see Synthetic data: simulating dynamic higher-order correlations. All estimates represented in this figure were computed using a Laplace kernel (width = 20). **Constant.** These datasets have stable (unchanging) underlying second-order correlation matrices. **Random.** These datasets are generated using a new independently drawn second-order correlation matrix at each timepoint. **Ramping.** These datasets are generated by smoothly varying the underlying second-order correlations between the randomly drawn correlation matrices at the first and last timepoints. **Event.** These datasets are each generated using five randomly drawn second-order correlation matrices that each remain stable for a fifth of the total timecourse. The vertical lines denote event boundaries. Note that the “dips” and “ramps” at the boundaries of sharp transitions (e.g., the beginning and ends of the “constant” and “ramping” datasets, and at the event boundaries of the “event” datasets) are finite-sample effects that reflect the reduced numbers of samples that may be used to accurately estimate correlations at sharp boundaries. Source data are provided as a Source Data file.

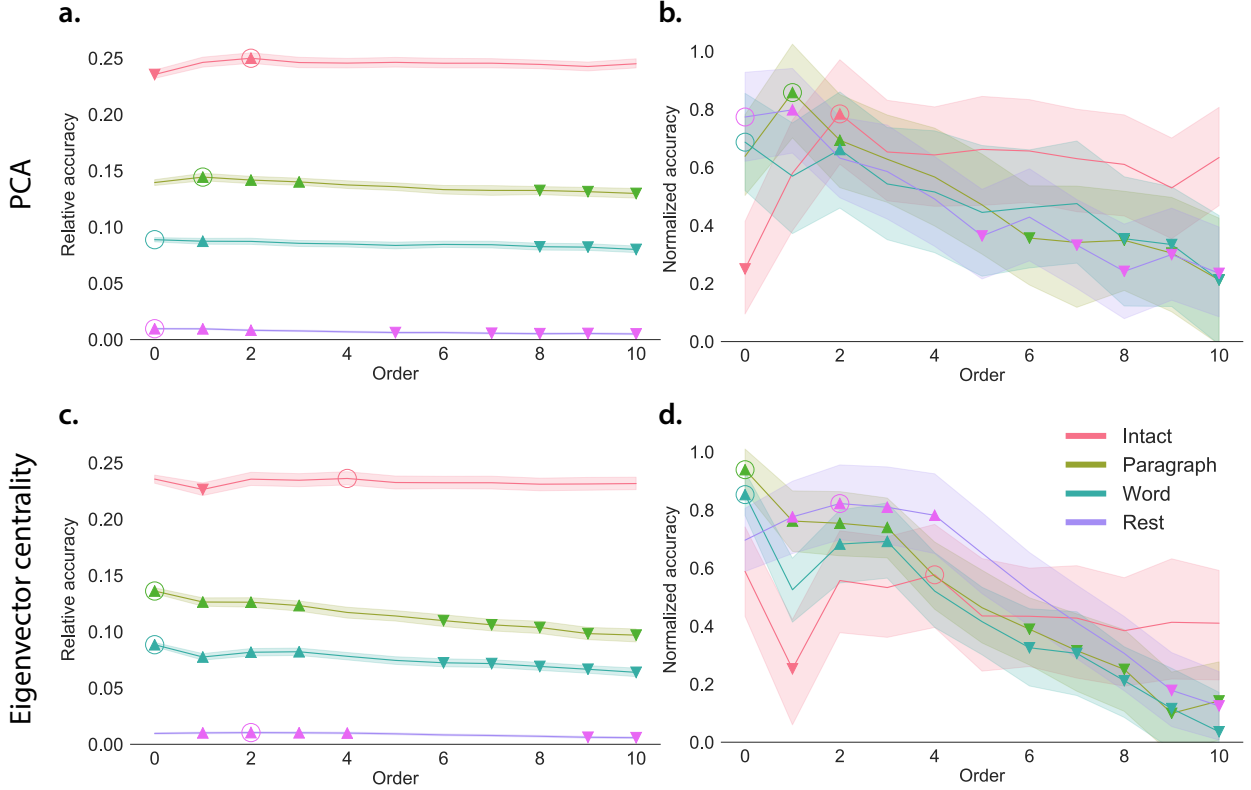


**Figure 4: Across-participant timepoint decoding accuracy varies with correlation order and cognitive engagement.**

**a. Decoding accuracy as a function of order: PCA.** “Order” (x-axis) refers to the maximum order of dynamic correlations that were available to the classifiers (see Feature weighting and testing). The reported across-participant decoding accuracies are averaged over all kernel shapes and widths (see Identifying robust decoding results). The y-values are displayed relative to chance accuracy (intact:  $\frac{1}{300}$ ; paragraph:  $\frac{1}{272}$ ; word:  $\frac{1}{300}$ ; rest:  $\frac{1}{400}$ ; these chance accuracies were subtracted from the observed accuracies to obtain the relative accuracies reported on the y-axis). The error ribbons denote 95% confidence intervals of the means across cross-validation folds (i.e., random assignments of participants to the training and test sets). The colors denote the experimental condition. Arrows denote sets of features that yielded reliably higher (upward facing) or lower (downward facing) decoding accuracy than the mean of all other features (via a two-tailed *t*-test, thresholded at  $p < 0.05$ ). Figure 5 displays additional comparisons between the decoding accuracies achieved using different sets of neural features. The circled values represent the maximum decoding accuracy within each experimental condition.

**b. Normalized timepoint decoding accuracy as a function of order: PCA.** This panel displays the same results as Panel a, but here each curve has been normalized to have a maximum value of 1 and a minimum value of 0 (including the upper and lower bounds of the respective 95% confidence intervals of the mean).

**c. Timepoint decoding accuracy as a function of order: eigenvector centrality.** This panel is in the same format as Panel a, but here eigenvector centrality has been used to project the high-dimensional patterns of dynamic correlations onto a lower-dimensional space.

**d. Normalized timepoint decoding accuracy as a function of order: eigenvector centrality.** This panel is in the same format as Panel b, but here eigenvector centrality has been used to project the high-dimensional patterns of dynamic correlations onto a lower-dimensional space. See Figures S1 and S2 for decoding results broken down by kernel shape and width, respectively. Source data are provided as a Source Data file.

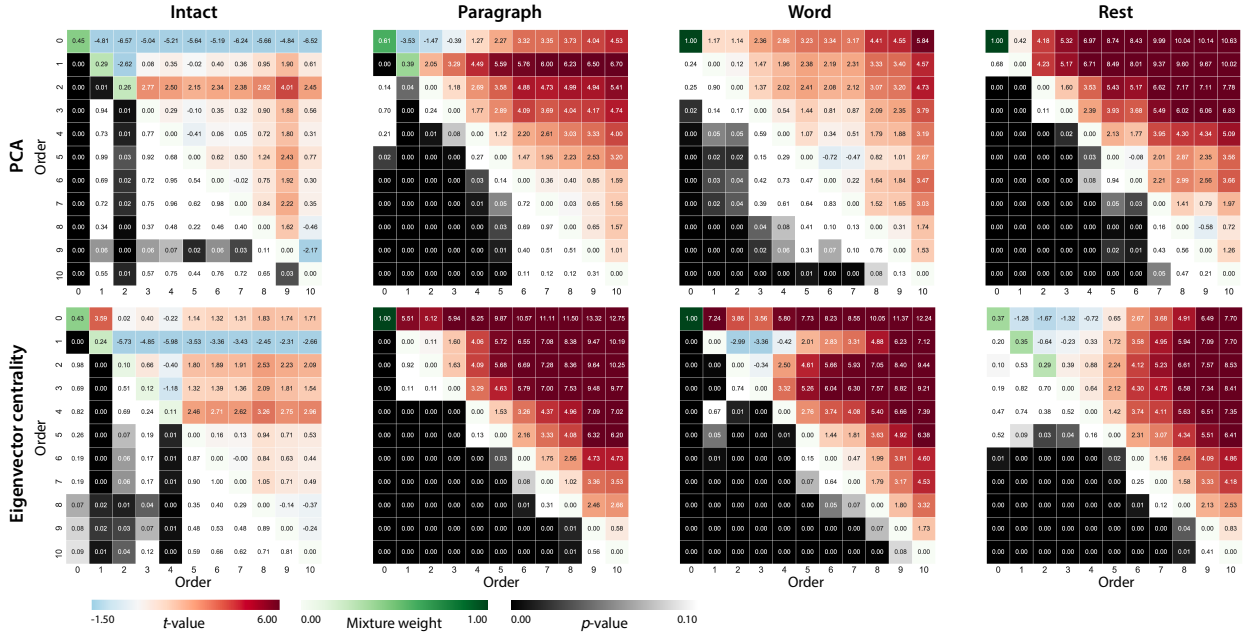


**Figure 5: Statistical summary of decoding accuracies for different neural features.** Each column of matrices displays decoding results for one experimental condition (intact, paragraph, word, and rest). We considered dynamic activity patterns (order 0) and dynamic correlations at different orders (order > 0). We used two-tailed  $t$ -tests to compare the distributions of decoding accuracies obtained using each pair of features. The distributions for each feature reflect the set of average decoding accuracies (across all kernel parameters), obtained for each random assignment of training and test groups. In the upper triangles of each matrix, warmer colors (positive  $t$ -values) indicate that the neural feature indicated in the given row yielded higher accuracy than the feature indicated in the given column. Cooler colors (negative  $t$ -values) indicate that the feature in the given row yielded lower decoding accuracy than the feature in the given column. The lower triangles of each map denote the corresponding  $p$ -values for the  $t$ -tests. The diagonal entries display the relative average optimized weight given to each type of feature in a decoder that included all feature types (see Feature weighting and testing). Source data are provided as a Source Data file.

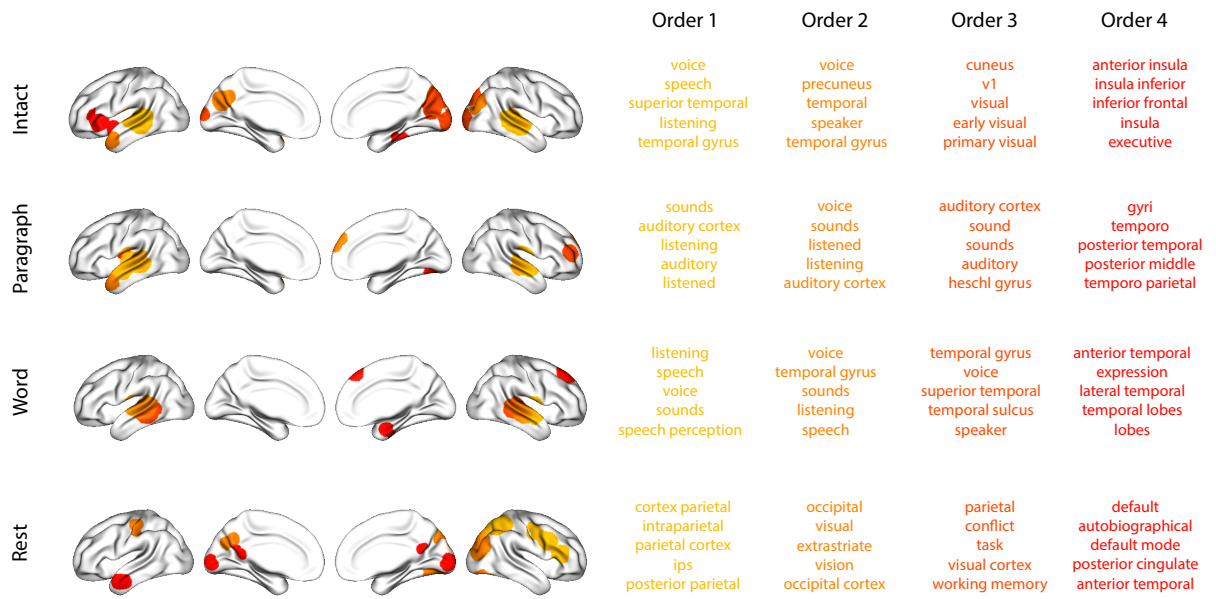


**Figure 6: Top terms associated with the most strongly correlated nodes at each order.** Each color corresponds to one order of inter-subject functional correlations. To calculate the dynamic correlations, eigenvector centrality has been used to project the high-dimensional patterns of dynamic correlations onto a lower-dimensional space at each previous order, which allows us to map the brain regions at each order by retaining the features of the original space. The inflated brain plots display the locations of the endpoints of the 10 strongest (absolute value) correlations at each order, thresholded at 0.999, and projected onto the cortical surface<sup>90</sup>. The lists of terms on the right display the top five Neurosynth terms<sup>38</sup> decoded from the corresponding brain maps for each order. Each row displays data from a different experimental condition. Additional maps and their corresponding Neurosynth terms may be found in the Supplementary materials (intact: Fig. S5; paragraph: Fig. S6; word: Fig. S7; rest: Fig. S8). Source data are provided as a Source Data file.

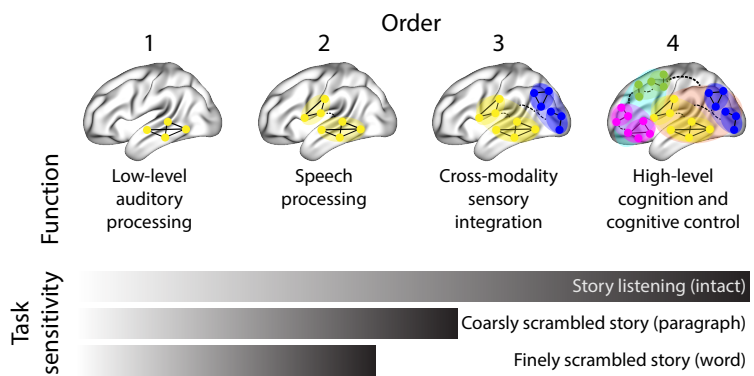


**Figure 7: Proposed high-order network dynamics underlying high-level cognition during story listening.** Schematic depicts higher orders of network interactions supporting higher-level aspects of cognitive processing. When tasks evoke richer, deeper, and/or higher-level processing, this is reflected in higher-order network interactions.

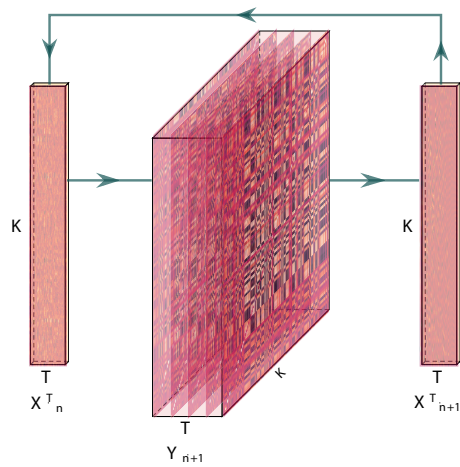


**Figure 8: Estimating dynamic high-order correlations.** Given a  $T$  by  $K$  matrix of multivariate timeseries data,  $\mathbf{X}_n$  (where  $n \in \mathbb{N}, n \geq 0$ ), we use Equation 4 to compute a timeseries of  $K$  by  $K$  correlation matrices,  $\mathbf{Y}_{n+1}$ . We then approximate  $\mathbf{Y}_{n+1}$  with the  $T$  by  $K$  matrix  $\mathbf{X}_{n+1}$ . This process may be repeated to scalably estimate iteratively higher-order correlations in the data. Note that the transposes of  $\mathbf{X}_n$  and  $\mathbf{X}_{n+1}$  are displayed in the figure for compactness.

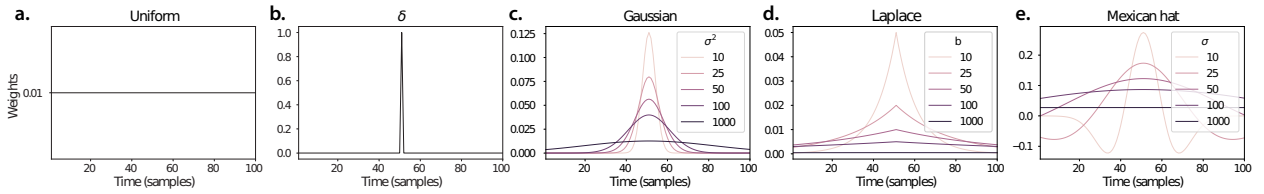


**Figure 9: Examples of kernel functions.** Each panel displays per-timepoint weights for a kernel centered at  $t = 50$ , evaluated at 100 timepoints ( $\tau \in [1, \dots, 100]$ ). **a. Uniform kernel.** The weights are timepoint-invariant; observations at all timepoints are weighted equally, and do not change as a function of  $\tau$ . This is a special case kernel function that reduces dynamic correlations to static correlations. **b. Dirac  $\delta$  kernel.** Only the observation at timepoint  $t$  is given a non-zero weight (of 1). **c. Gaussian kernels.** Each kernel's weights fall off in time according to a Gaussian probability density function centered on time  $t$ . Weights derived using several different example width parameters ( $\sigma^2$ ) are displayed. **d. Laplace kernels.** Each kernel's weights fall off in time according to a Laplace probability density function centered on time  $t$ . Weights derived using several different example width parameters ( $b$ ) are displayed. **e. Mexican hat (Ricker wavelet) kernels.** Each kernel's weights fall off in time according to a Ricker wavelet centered on time  $t$ . This function highlights the contrasts between local versus surrounding activity patterns in estimating dynamic correlations. Weights derived using several different example width parameters ( $\sigma$ ) are displayed.

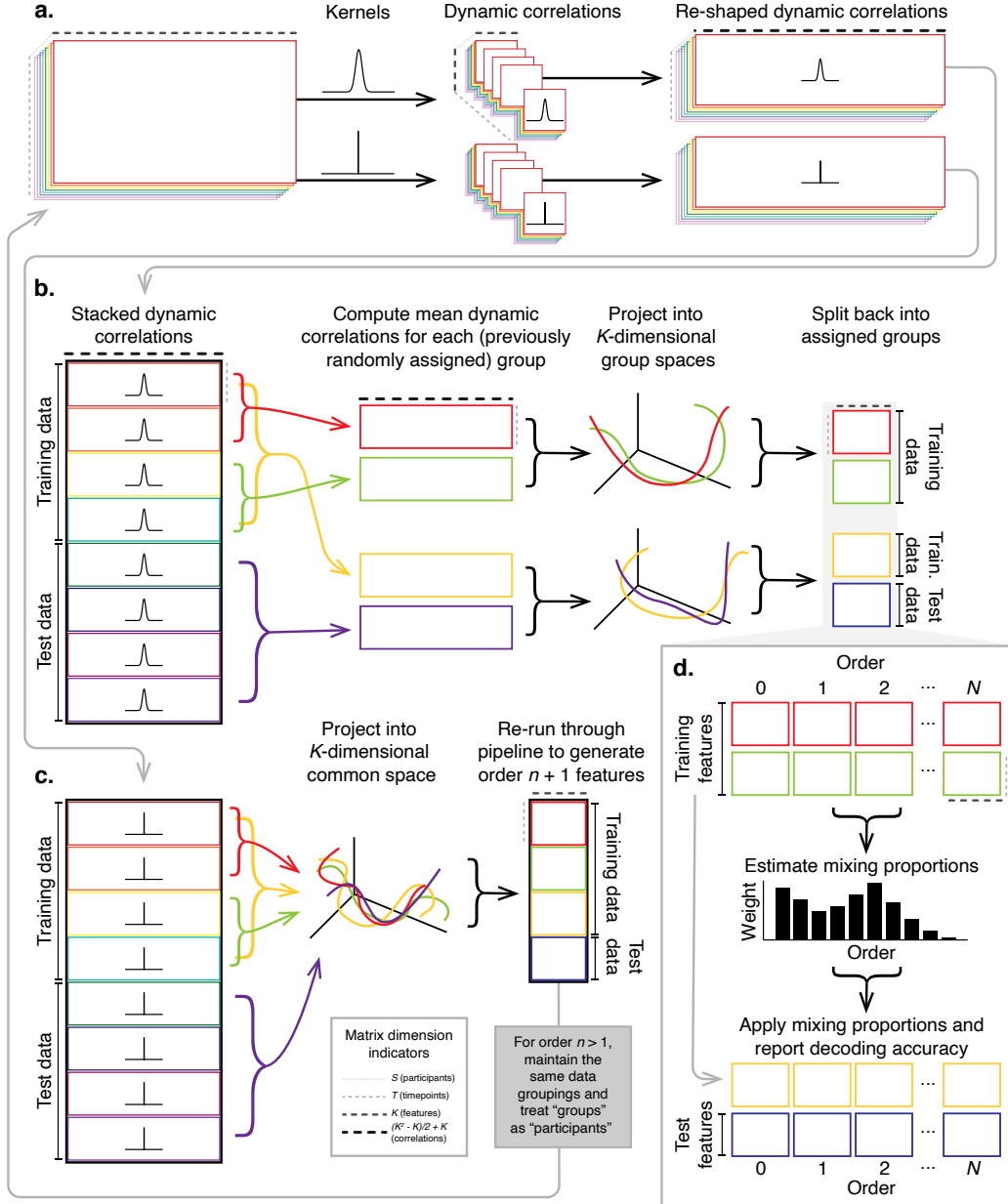


**Figure 10: Decoding analysis pipeline.** **a. Computing dynamic correlations from timeseries data.** Given a timeseries of observations as a  $T \times K$  matrix (or a set of  $S$  such matrices), we use Equation 4 to compute each participant's DISFC (relative to other participants in the training or test sub-group, as appropriate). We repeat this process twice—once using the analysis kernel (shown here as a Gaussian in the upper row of the panel), and once using a  $\delta$  function kernel (lower row of the panel). **b. Projecting dynamic correlations into a lower-dimensional space.** We project the training and test data into  $K$ -dimensional spaces to create compact representations of dynamic correlations at the given order (estimated using the analysis kernel). **c. Kernel trick.** We project the dynamic correlations computed using a  $\delta$  function kernel into a common  $K$ -dimensional space. These low-dimensional embeddings are fed back through the analysis pipeline in order to compute features at the next-highest order. **d. Decoding analysis.** We split the training data into two equal groups, and optimize the feature weights (i.e., dynamic correlations at each order) to maximize decoding accuracy. We then apply the trained classifier to the (held-out) test data.